

Numerical study on dual oscillating wave surge converter with different cross-section shapes using SPH under regular waves

Jie Cui^a, Xin Chen^a, Saishuai Dai^{b,*1}

a School of naval architecture and ocean engineering, Jiangsu University of Science and Technology, Zhenjiang, 212003, China

b Naval Architecture, Ocean and Marine Engineering Department, University of Strathclyde, Glasgow, United Kingdom

Abstract

The Oscillating Wave Surge Converter (OWSC) has been widely adopted in energy extraction from sea waves in recent years, particularly in relatively shallow water areas. In this research work, the wave energy absorption efficiency of dual OWSCs with various cross-section shapes, including diamond-shaped flap, cylindrical flap, elliptical flap, and rectangular flap, were investigated using a coupled numerical model between SPH and chrono-engine. A single OWSC was also numerically examined for comparison. In addition to the comparison between a single unit and dual flap OWSCs, design parameters like the interval between the two flaps, wave conditions, the water depth, and the linear PTO damping were also examined in this work. The numerical results suggest that the rectangular flap performs better in energy extraction than the other flap shapes under most wave conditions. Besides, the distances between the two flaps significantly affect energy extraction. In addition, results further suggest that the energy performance will drop when the distance between the two flaps equals one wavelength. Furthermore, the submerged depth of the flap structure plays an important role in wave energy extraction. When the flap height is less than the water depth, the wave energy efficiency increases at the beginning and then decreases as the linear PTO system increases. If the flap height is more than the water depth, the energy extraction performance of the dual OWSC can

*Corresponding author: Saishuai Dai

Email:saishuai.dai@strath.ac.uk

be significantly improved.

Keywords: dual OWSCs, various cross-section shapes, SPH method, wave energy extraction

1. Introduction

Among all the promising marine renewable energy resources, wave energy is increasingly gaining popularity for its predictability, longer available time, and higher energy density (Gunn and Stock-Williams, 2012). Despite the above merits, wave energy is still less competitive in terms of the Levelised Cost of Energy compared with alternative energy resources (both renewable and non-renewable) (Astariz and Iglesias, 2015). The LCOE is defined as the net present value of the unit cost of electricity over the lifetime of a device, and it is typically given as cost per megawatt-hour. For example, onshore and offshore wind costs are 67.68 €/MWh and 101.43 €/MWh, respectively. In the case of wave energy, the cost ranges from 90 to 490 €/MWh, depending on technologies. It is, therefore, critical for wave energy technologies to reduce their current LCOE to achieve commercial viability. Several plausible pathways to achieve a lower LCOE have been proposed in the past years, including creating synergies by sharing infrastructures with other marine applications (Caitlyn et al., 2019), identifying new materials and structural designs to lower the capital cost (Netbuoy, 2021), etc. Accurate assessment and optimisation of a Wave Energy Converter (WEC) can reduce LCOE by accurately estimating annual energy production and providing more efficient design/configuration solutions.

Extensive studies have investigated the performance of WECs in the past decade. For example, Babarit (2015) established a database for the hydrodynamic performance of various wave energy converters, including bottom fixed heave buoy array, floating heave buoy array, and oscillating wave surge converter aiming to derive an annual average for the capture width ratio of the different technologies. Among all the different types of WECs, not only the Oscillating Wave Surge Converter (OWSC) has attracted many scholars' attention due to its simpler working principle and higher efficiency, but also Oscillating Water Column (OWC) system has been one of the most influential wave energy converter types (Simonetti et al., 2018;

Wang et al., 2018). Çelik and Altunkaynak (2018) designed physical experiments of a fixed Oscillating Water Column (OWC) system with seven different sizes of opening heights. Then mathematical models were proposed to predict water column fluctuations under varying relative opening heights and wave parameters. The highest relative average column water surface fluctuations were found and the accuracy of mathematical models was verified by the model tests. While the hydrodynamic performance of the OWC system is beyond the scope of the work. In this research work, the OWSC system has been chosen as the main research object. Particularly bottom fixed type OWSC, which is suitable for deployment near coastal areas. Such a device arrangement can provide coast protection alongside green and renewable energy production, e.g. extracting energy from waves dampens the wave height at the same time.

The mechanisms and characteristics of an OWSC were investigated by Henry et al. (2014a) both numerically and experimentally. It was concluded that the maximum pressure occurred at the center of the flap. Schmitt et al. (2016a) developed a numerical methodology that couples the open-source boundary element code NEMOH with a Finite Element Analysis (FEM) tool called CodeAster. The experimentally validated numerical tool successfully captured the natural frequencies and mode shapes of an OWSC. By both numerical simulations and experiments, Wei et al. (2015) found that the hydrodynamic forces (excitation, diffraction, and radiation force) dominate the motion response of an OWSC and the viscous effect is less important. The slamming process and the flap dynamics of an OWSC were also discussed by Wei et al. (2016). Their results suggest that the highest impact pressure occurred at the middle of the flap below the mean water level. Similar work was also conducted by Cheng et al. (2018) and Renzi et al. (2018). Including geometric configurations (Liu et al., 2020), power take-off damping levels (Schmitt et al., 2016b; Jiang et al., 2018), and wave conditions (Brito et al., 2020). Gunawardane et al. (2019) analysed and compared four different OWSC variants systematically. An effective method was developed to investigate the differences in the hydrodynamic performance of all the proposed variants. Besides, an analytical 3D model was

developed to study the interaction between tsunamis and an OWSC based on the nonlinear shallow water equations and empirical formulas (O'Brien et al., 2015). In addition to a single unit of OWSC, many scholars have investigated the interaction between dual OWSCs (Renzi et al., 2014; Greenwood et al., 2016). Cheng et al. (2021) established a coupled three-dimensional hydrodynamic model of dual-OWSCs based on the potential flow theory with fully nonlinear boundary conditions in the time domain. The numerical simulation demonstrated that a staggering array system could increase wave energy extraction in the resonance region. Similarly, Tay and Venugopal (2017) used the industry-standard hydrodynamic software WAMIT to examine the power production of multiple OWSCs under various wave conditions, including regular waves, unidirectional irregular waves, and multi-directional sea. It was found that the wave energy conversion of the OWSCs was greatly influenced by the spreading function, the resonance bandwidth, and the optimal spacing between the devices.

Most of the above numerical studies were carried out using the well-known inviscous and irrotational linear potential theory. Except for this, many scholars had proposed some theory and found that many of the more valuable concerns by restrict theoretic analysis and model inference, which has a significant influence on OWSCs or WEC design. Michele et al. (2015) considered a flap gate motion forced by monochromatic incident waves which can be fundamental for the optimisation of the gate farm for energy production. And Michele et al. (2016a) investigated the diffraction and radiation potentials of a finite array of floating flap gates OWSC by solving in terms of elliptical coordinates and Mathieu functions. Similarly, a semi-analytical theory was given for “non-thin” gate geometry by Michele et al.(2016b). A second-order nonlinear theory was proposed by Michele (2018a; 2019), which was intended for curved wave energy converters design. The theoretical analysis indicated that hydrodynamic interactions between the curved gate and waves could have either positive or negative effects on power absorption. Michele et al. (2018b) presented a weakly nonlinear theory about the natural modes' resonance of an array of oscillating wave surge converters (OWSCs) in a channel and investigated its performance

theoretically. Additionally, it also was proved that the subharmonic resonance could improve the wave energy capture efficiency of OWSCs in a significant way. After that Michele et al. (2019) applied a weakly nonlinear theory to surging wave energy converters (WECs) with curved geometry and the related results have shown the effects of nonlinear synchronous resonance were also the key factor of surging wave energy converter design. Moreover, contrary to conventional offshore structures, wave energy devices are designed to maximise the interaction with waves. Strong non-linearity and turbulence are therefore expected. Linear potential theory-based simulations often cannot accurately assess the performance of a wave energy device, especially around the natural frequency region where the response reaches the maxima. Compared with potential flow theory, CFD methodologies like the Finite Volume Method (FVM) and Smooth Particle Hydrodynamics (SPH) methods can address the strongly nonlinear wave-WEC interaction problem with improved accuracy. FVM-based CFD methods often require a significant amount of computation resources due to the requirement of extra dense mesh around the free surface and structure. On the other hand, the SPH method is meshless (despite the requirement of a considerable number of particles). Many open-source SPH codes have recently, such as SPHinXsys (Zhang et al., 2021). Among all the codes, DualSPHysics has been widely used in ocean engineering owing to its accuracy (Altomare et al., 2017; Crespo et al., 2011; Cui et al., 2021) and highly optimised code structure, which can significantly reduce the total cost of the simulation (Domínguez et al., 2019; Altomare et al., 2014). In this research work, DualSPHysics is selected as the main numerical tool to predict the coupling process between the nonlinear waves and flap motion of the OWSCs.

Liu et al. (2021) optimised the configuration of an array of OWSCs by using a novel analytical wave model based on the SPH method and differential evolution algorithms. Their numerical simulation suggests that the proposed array layout can improve the overall energy extraction efficiency. Zhang et al. (2018) applied the SPH method to investigate the hydrodynamic characteristics of a land-hinged OWSC. Results indicate that the PTO damping coefficients and the wave periods played a

critical role in the power extraction of the land-hinged OWSC.

The above studies have focused on either geometry optimisation for a single OWSC or layout optimisation for multiple simple OWSCs. The effect of geometry optimisation on dual/multiple OWSCs is not well understood. The current study investigates a dual OWSCs system with four different flap shapes using the SPH method. Their power extraction performance is compared against single units with their corresponding flap shapes. Parameters like water depth, the separation distance between flaps, and the damping level of the PTO system are also studied. The rest of the study is planned as follows: section 2 describes the numerical methods, followed by a validation and verification study in section 3. Section 4 presents the numerical simulation results, and conclusions are drawn in section 5.

2. Numerical model

In this research work, Project Chrono (Tasora et al. 2016; Project Chrono, 2018) is applied to couple with fluid solver (DualSPHysics: <https://dual.sphysics.org/>) for multibody dynamics simulation, which is available at <https://projectchrono.org/>. The coupling schedule has been designed and validated against tank testing of an OWSC (Brito et al., 2020). The implicit Euler method is implemented to solve ordinary differential equations (ODEs) in Project Chrono. The detailed coupling procedure between DualSPHysics and Chrono can be referred to in Canelas (2018).

2.1 SPH governing equations

SPH method is a Lagrange solver developed to resolve free-surface flow problems or wave-structure interaction. The entire computational domain is discretised into a set of material points or particles. The discretised Navier-Stokes equations are then locally integrated at the position of each of these particles according to the nature of neighbouring particles. The dynamics of these particles are governed by the continuity and momentum equations (Becker and Teschner, 2007) in the Lagrangian form, which can be expressed as follows:

$$\frac{d\rho_i}{dt} = \rho_i \sum_{k=1}^N \frac{m_k}{\rho_k} \mathbf{v}_{ik} \cdot \nabla_i W_{ik}, \quad (1)$$

$$\frac{d\mathbf{v}_i}{dt} = -\sum_k m_k \left(\frac{P_k}{\rho_k^2} + \frac{P_i}{\rho_k^2} + \Pi_{ik} \right) \nabla_i W_{ik} + \mathbf{g}, \quad (2)$$

where ρ is the fluid density, \mathbf{g} and m represent the gravity acceleration and the particle mass, respectively. ∇_i is the gradient of the kernel taken with respect to the coordinates of particle i . The subscripts i and k denotes the target particle and its surrounding particle, respectively. \mathbf{v}_i indicates the velocity vector and $W_{ij} = W(|\mathbf{r}_i - \mathbf{r}_k|, h)$ is the kernel function, where \mathbf{r}_i and \mathbf{r}_k represent particle positions. In this paper, the Wendland kernel function was used (Wendland, 2015). The Cole equation of state is adapted to provide a closure relation for pressure P (Monaghan et al., 1999; Batchelor, 1974):

$$p = \xi \left[(\psi)^\gamma - 1 \right], \quad (3)$$

with $\psi = \rho / \rho_0$ and $\xi = c_0^2 \rho_0 / \gamma$, respectively. where γ is a dimensionless coefficient, ρ_0 indicates the fluid reference density. According to Gomez-Gesteira et al. (2012), $\gamma = 7$ and $\rho_0 = 1000 \text{ kg/m}^3$. c_0 denotes the speed of sound, which can be used to control the density variations within the limits imposed by stability criteria. And the sound speed is always lower than the physical sound, which can reduce the computational cost. According to Antuono (2011), the flow velocity is usually at a low level and in that case, the wave celerity ($c = \sqrt{\mathbf{g}H_{depth} \left(\tanh(kH_{depth}) / kH_{depth} \right)}$) is the key influencing factor with H_{depth} is the still water depth of the computational domain during the wave propagation. It should be noted that $\tanh(kH_{depth})$ is approximately equal to kH_{depth} in the shallow water regime. So in this research work, we chose the upper bound for the wave celerity ($c = \sqrt{\mathbf{g}H_{depth}}$) and the speed of sound c_0 is equal to $10c$ which can satisfy these requirements in the weakly compressible SPH (WCSPH) method.

Additionally, following the work by Monaghan (1992), an artificial viscosity term Π_{ik} is added to the momentum equation, and the equation reads:

$$\Pi_{ik} = \begin{cases} \frac{-\alpha \overline{c_{ik}} \mu_{ik}}{\rho_{ik}} & \text{if } \mathbf{v}_{ik} \cdot \mathbf{r}_{ik} < 0 \\ 0 & \text{else } \mathbf{v}_{ik} \cdot \mathbf{r}_{ik} > 0 \end{cases}, \quad (4)$$

$$\mu_{ik} = \frac{h \mathbf{v}_{ik} \cdot \mathbf{r}_{ik}}{\mathbf{r}_{ik}^2 + \eta^2}, \quad (5)$$

with $\mathbf{v}_{ik} = \mathbf{v}_i - \mathbf{v}_k$, $\mathbf{r}_{ik} = \mathbf{r}_i - \mathbf{r}_k$ and $\eta^2 = 0.01h^2$. Moreover, $\overline{c_{ik}} = (c_i + c_k)/2$ represents the mean speed of sound at the locations of particles i and k , and $\alpha = 0.01$ (Altomare et al., 2015).

A corrective term, the density diffusive term (Antuono et al., 2010), is applied in the continuity equation to minimise the high-frequency low-amplitude oscillations which result from the natural disorder of the Lagrangian particles. As a note, the density diffusive term should be convergent all over the fluid domain and keep the mass and momentum conserve exactly (Antuono et al., 2012).

Firstly, a brief proof of the conservative density diffusive term is presented as follows (Antuono et al., 2010). A term $\Gamma(\mathbf{r})$ is added in the continuity equation (Eq.1). And the conservative principles should be maintained. So, the term can be written as:

$$\int_{\Omega} \Gamma(\mathbf{r}) dV = 0, \quad (6)$$

when it is discretised, Eq. 6 can be written as:

$$\sum_i \Gamma_i dV_i = 0, \quad (7)$$

where Γ_i can be replaced by:

$$\sum_k \psi_{ik} \cdot \nabla_i W(\mathbf{r}_k) dV_k, \quad (8)$$

where ψ_{ik} is symmetric functions ($\psi_{ik} = \psi_{ki}$) and $\nabla_i W(\mathbf{r}_k)$ is antisymmetric ($\nabla_i W(\mathbf{r}_k) = -\nabla_k W(\mathbf{r}_i)$). So Eq. 7 can be satisfied. More details can be referred to in Antuono et al. (2010). The detailed convergence analysis can also be found in Antuono et al. (2010) and Antuono et al. (2012).

Thus, the corrective continuity equation is given by (Marrone et al., 2011):

$$\frac{d\rho_i}{dt} = \sum_k m_k \mathbf{v}_{ik} \cdot \nabla_i W_{ik} + \delta h c_0 \sum_k \psi_{ik} \cdot \nabla_i W_{ik} \frac{m_k}{\rho_k}, \quad (9)$$

$$\psi_{ik} = 2(\rho_k - \rho_i) \frac{\mathbf{r}_{ki}}{(\mathbf{r}_{ik})^2} \cdot \left[\langle \nabla \rho \rangle_i^L + \langle \nabla \rho \rangle_k^L \right], \quad (10)$$

with a constant coefficient $\delta = 0.1$. The renormalised density gradient $\langle \nabla \rho \rangle^L$

(Randles et al., 1996) can be given as:

$$\begin{cases} \langle \nabla \rho \rangle_i^L = \sum_k (\rho_k - \rho_i) \mathbf{L}_i \nabla_i W_{ik} \frac{m_k}{\rho_k} \\ \mathbf{L}_i = \left[\sum_k (\mathbf{r}_k - \mathbf{r}_i) \otimes \nabla_i W_{ik} \frac{m_k}{\rho_k} \right]^{-1}, \end{cases} \quad (11)$$

Meanwhile, the particle shifting technique (PST (Lind et al., 2012)) was adopted to regularise particle distributions and solve negative pressure or unphysical flow voids (Sun et al. (2018)). The details of those methods can be referred to in the research work of Mokos et al. (2016) for multiphase SPH simulations.

2.2 Boundary conditions

The dynamic Boundary Condition (DBC) (Crespo et al., 2007) method is selected to treat the boundaries, where the boundary particles follow the same governing equations of continuity and state as the fluid particles. Unlike the fluid particles, the boundary particles cannot move according to the forces acting on them: they remain either fixed or move according to a predefined movement. The main advantage of this boundary treatment is that it can deal with complex geometries easily and provides higher computational efficiency. Simultaneously, a flap-type wavemaker is preinstalled at one side of the numerical wave tank to generate waves according to a second-order wave generation theory (Madsen, 1971). A damping zone is defined at the other side of the numerical wave tank to avoid wave reflection (Altomare et al., 2017).

2.3 Flap motion of OWSC

Normally in the single-phase SPH method framework, the categories of particles

have been grouped into two types, including fluid particles and solid particles. In this paper, the flap structure is treated as a rigid body, neglecting the elastic deformation. In that case, taking the external force (\mathbf{F}_{ch}) and torque (τ_{ch}) applied to the hinge computed by the Chrono library, the discretised Newton's equations for rigid body dynamics are applied to resolve the dynamic responses of floating structure (Canelas et al., 2015; Crespo et al., 2015):

$$M \frac{d\mathbf{V}}{dt} = \sum_{b \in \text{boundary}} m_b \mathbf{f}_b + \mathbf{F}_{ch}, \quad (12)$$

$$I \frac{d\boldsymbol{\Omega}}{dt} = \sum_{b \in \text{boundary}} m_b (\mathbf{r}_b - \mathbf{C}) \times \mathbf{f}_b + \tau_{ch} - \nu_{pto} \boldsymbol{\Omega}, \quad (13)$$

where M denotes the floating structure's total mass, \mathbf{V} is the velocity, m_b is the mass of the flap structure particle b , \mathbf{f}_b is the force by unit mass applied to the flap structure particle b . I is the moment of inertia of the structure. $\boldsymbol{\Omega}$ represents the rotational velocity. \mathbf{r}_b is the position of the flap structure particle b . \mathbf{C} is the center of mass. ν_{pto} is the damping of the PTO. The velocity of the flap structure particle b can be obtained by integrating Eq. (12) and Eq. (13) over time:

$$\mathbf{v}_b = \mathbf{V} + \boldsymbol{\Omega} \times (\mathbf{r}_b - \mathbf{C}), \quad (14)$$

2.4 Wave energy capture factor

The performance of an OWSC can be accessed by the so-called capture factor. The capture factor is defined as the ratio between the power extracted by a WEC and the incident wave power. For a single OWSC, the time-averaged power extracted by the linear PTO system (P_e) can be written as (Henry et al., 2018; Brito et al., 2020):

$$P_e = \frac{1}{2} \varpi^2 \nu_{pto} |\theta_w^2|, \quad (15)$$

$$CF = \frac{P_e}{E_i C_g B}, \quad (16)$$

where ϖ denotes the angular frequency of the incoming waves. θ_w is the flap rotation amplitude. CF is the capture factor, B is the width of the flap (In 2D simulations, B

is usually set to 1), and the term $E_i C_g$ can be written as:

$$E_i C_g = \frac{\rho g H^2 \omega}{16k} \left(1 + 2 \frac{kd}{\sinh(2kd)} \right), \quad (17)$$

where E_i is the time-averaged energy of unit width regular incident waves, H is the incident wave height, k is the wave number, and d is the water depth.

C_g represents the group velocity and more details can be referred to in Mei et al. (2005). When there are two or more OWSCs in the flow fields, and they are subjected to the same wave actions simultaneously, the total time-averaged captured power can be calculated as the algebraic summation of the time-averaged power for all OWSCs.

3 Convergence test and validation of the SPH model

Based on the recurrence of the representative OWSC experiments (Wei et al., 2016), the validation and convergence of the SPH method are demonstrated in this section. The optimum particle resolution was decided by considering the computation time and the accuracy through convergence analysis. All the simulations of numerical cases were accelerated by an NVIDIA GeForce RTX 3090 GPU card.

3.1 Numerical setup

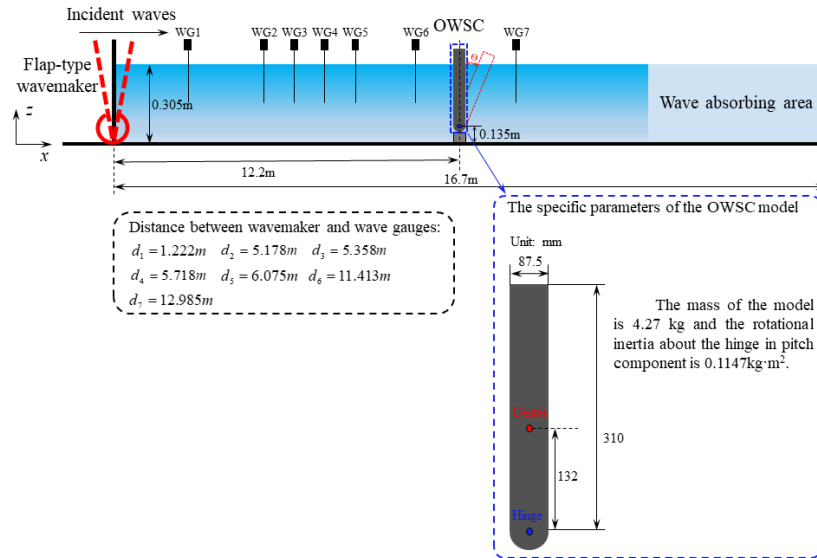


Fig. 1. The schematic diagram of the arrangement of the experiment model and measured points (Wei et al., 2016)

The layout of Wei's experiment is shown in Fig. 1. The schematic diagram of the arrangement of the experiment model and measured points (Wei et al., 2016), including the size of the wave flume, the positions of wave gauges, and the

dimensions of the physical OWSC model. The physical wave tank is 16.7m long, 0.65m wide, and the water depth is set to 0.30 m. A flap-type wavemaker is installed at one side, and a wave beach is arranged on the other side of the tank. Seven wave probes are allocated along the wave propagation direction to measure wave elevations. The OWSC model tested has a scale factor of 1:40th. More detailed information on the model, including the mass properties, can be found in Table.1.

The Numerical Wave Tank (NWT) used the same tank dimensions apart from the wave beach. A damping zone is employed to absorb the incoming waves instead of physically modelling the physical porous media in the physical wave tank. In this section, the wave height and wave period of incident waves are 0.1m, and 1.9s, respectively.

3.2 Convergence analysis

In this section, a series of convergence analyses were conducted for the examined model, where different initial interparticle distances were used in the numerical simulations, such as $d_p = 0.008m$, $d_p = 0.005m$, $d_p = 0.002m$, $d_p = 0.0015m$. Unlike other meshed software (Star-CCM+ et al.), the convergence analysis of the time steps was not carried out in this section because the initial time step can be set to zero in SPH simulation. The time step size was set by the CFL condition in each time step. In each simulation, both free-surface elevations and the flap response were recorded.

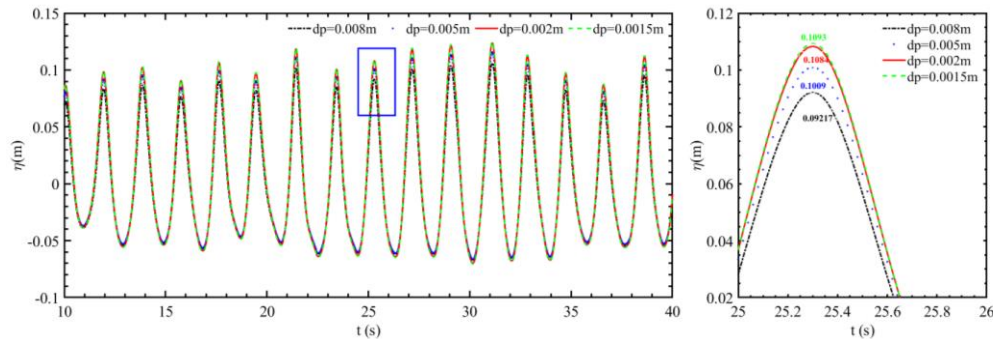


Fig. 2. Convergence tests of water elevations at WG5 with different particle distance schemes

The time history of water elevations measured at WG5 with different interparticle distances is given in Fig. 2. Convergence tests of water elevations at WG5 with

different particle distance schemes. Overall, all four simulations agree with each other well. The crest increased slightly with decreased interparticle distance. For example, at $t=25.3s$, just as shown in the right column of Fig. 2. Convergence tests of water elevations at WG5 with different particle distance schemes, the crest increased from 0.0922 m to 0.1009 m when the interparticle distance decreased from 0.008 m to 0.005 m. The crest increased further to 0.1084 when the distance was reduced to 0.002m. However, the crest only changed 0.8% when the distance was reduced to 0.015m, indicating the convergency is achieved at 0.002m. A similar trend can be observed in the flap rotation and angular velocity as illustrated in Fig. 3. Convergence tests of flap motions and flap angular velocity for the examined OWSC model with different particle distance schemes. (a) flap rotation; (b) flap angular velocity (a) and (b). In addition to smaller magnitudes, there is some phase delay in the response when the interparticle distance is greater than 0.002 m. No apparent phase difference is observed between the cases using 0.002m and 0.0015m. Just as shown in the right column of Fig. 3. Convergence tests of flap motions and flap angular velocity for the examined OWSC model with different particle distance schemes. (a) flap rotation; (b) flap angular velocity(a), the flap rotation amplitudes only increased 1.06% when the interparticle distance decreased from 0.002m to 0.0015m. Similarly, the flap angular velocity only changed 1.17% in that case. The wave elevation and the flap angular velocity indicate that the results varied by negligible amounts when the interparticle distance changed from 0.002 to 0.0015. On the other hand, the computational time grew substantially despite GPU acceleration when d_p decreased from 0.002 m to 0.0015m. For example, when d_p is set to 0.002m, the computation time is about 4h. However, it will take 12h to run the same simulation when d_p is set as 0.0015m. With a 1% increment, the computational time tripled. It is therefore decided to use 0.002 m as the interparticle distance for simulations hereafter.

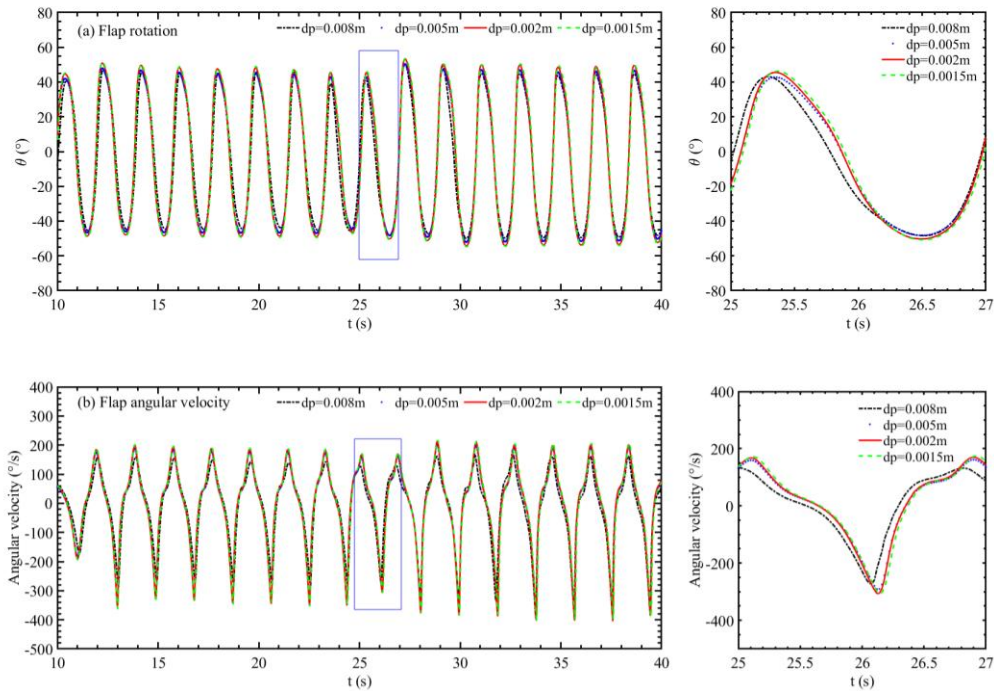


Fig. 3. Convergence tests of flap motions and flap angular velocity for the examined OWSC model with different particle distance schemes. (a) flap rotation; (b) flap angular velocity

3.3 Model validation

To validate the present SPH model, the simulation results are compared with the existing experimental data conducted by Wei et al. (2016). Fig. 4 presents the comparison of the water surface elevation data at WG5 between the SPH simulation and the experiments. The comparison of the flap rotation and the flap angular velocity for the OWSC model are presented in Fig. 5(a) and Fig. 5(b), respectively. It is worth mentioning that there exists some discrepancy between the SPH simulation result and the experiment result. As shown in Fig. 4, the experimental wave amplitudes are higher than that of the SPH simulation. A similar discrepancy is observed in simulations performed using ANSYS FLUENT (Wei et al., 2016). As described by Wei et al. (2016), the reasons for these small differences may be attributed to the time ramp used in experiments to generate waves gradually while this technology is not implemented in the numerical methods. Also, artificial numerical errors like numerical diffusion and numerical dissipation, which are not experienced in tank testing, contribute to the discrepancy as well. Overall, it can be seen from these figures that the currently proposed SPH simulation can study the OWSC

problem with good accuracy and stability.

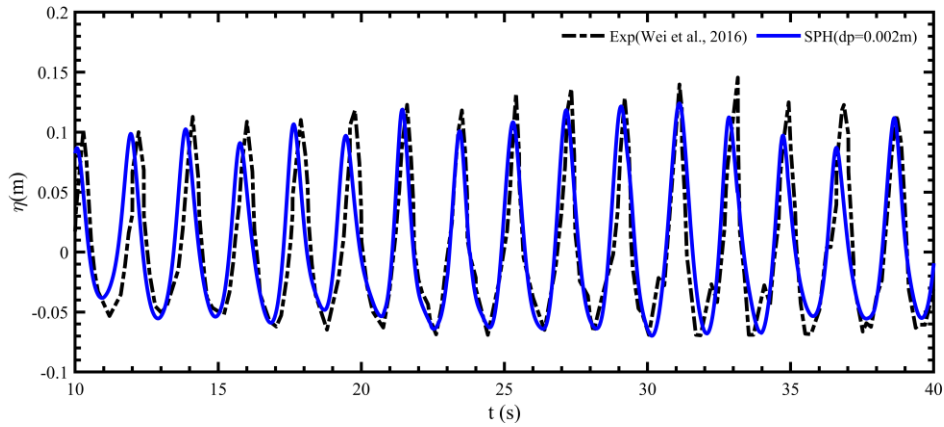


Fig. 4. Time series of water surface elevation for SPH simulation at WG5 in comparison with the experimental data in Wei et al. (2016)

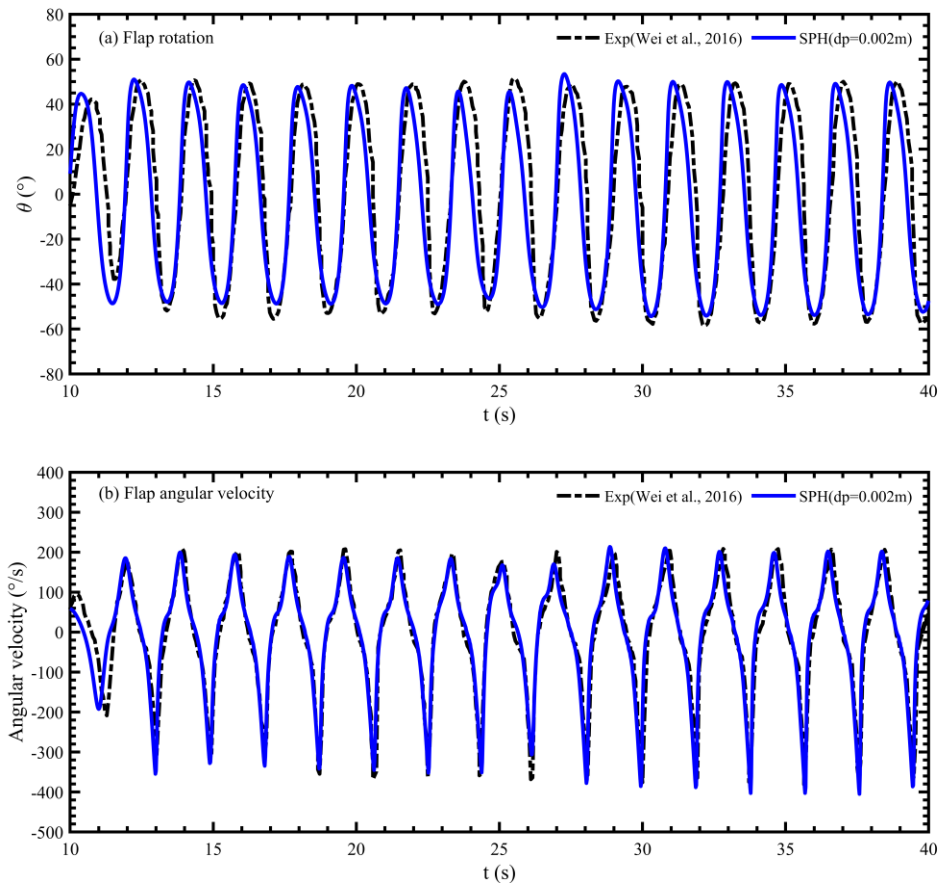


Fig. 5. Time series of (a) flap rotation and (b) flap angular velocity of the examined OWSC model for SPH simulation in comparison with the experimental data in Wei et al. (2016)

4. Numerical simulations and results

Although OWSCs are often deployed at a shallower site where wave breaking, slamming (Henry et al., 2014b), and other strongly nonlinear phenomena due to shallow water waves are often observed, the current study focus on the effect of

different cross-section shapes. Only intermediate-depth water waves are considered in this study. The shallow water wave effect will be investigated in future works. Three different water depths are examined in the current study. Six wave conditions are explored in the present simulations, and wave parameters can be found in **Table 1**.

A simplified process of OWSC’s cross-section shapes is listed in **Table 2**. For exploratory research purposes, there are subtle differences between some numerical models and engineering prototypes. **Table 3** tabulated the detailed dimension parameters of various shapes, including both the single flap and dual flaps. For a dual OWSC system, flap I represent the first flap closer to the wavemaker, and flap II is the second flap near the wave absorbing zone.

Apart from this, other parameters which can affect the wave energy capture capability of OWSCs, such as the PTO system and the distance between the two flaps are also discussed.

Table 1 Wave parameters for different water depth

Abbreviation of wave conditions	WC1	WC2	WC3	WC4	WC5	WC6
Wave height: H(m)	0.114	0.12	0.138	0.147	0.162	0.165
H / d_p	57	60	69	73.5	81	82.5
Wave period: T(s)	1.26	1.42	1.58	1.8	1.9	2.00
Water depth: h(m)	0.358		0.448		0.538	

Table 2 A simplified process of OWSC's cross-section shape


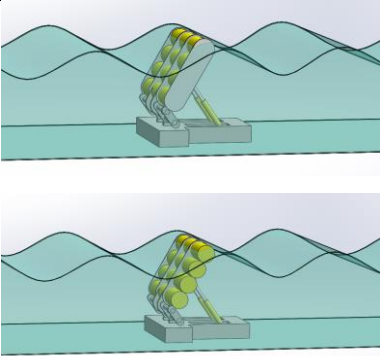
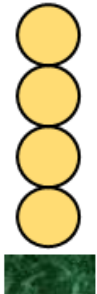

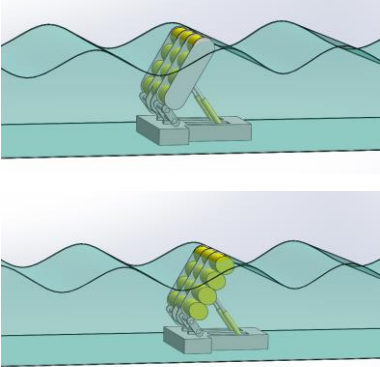
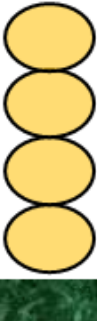

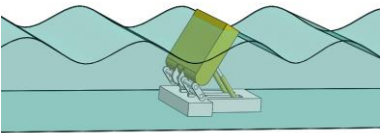
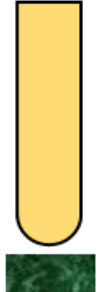

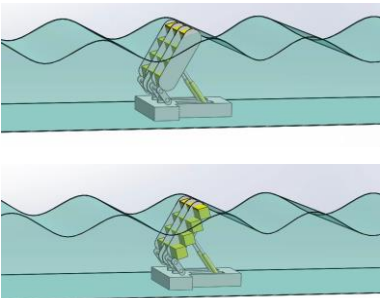

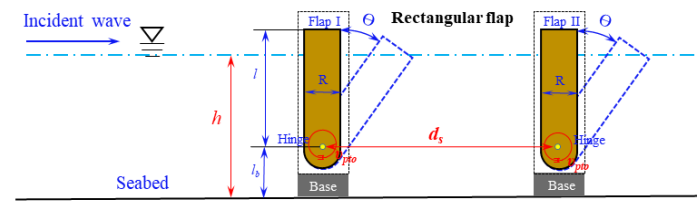
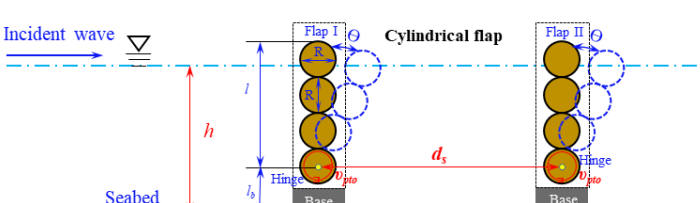
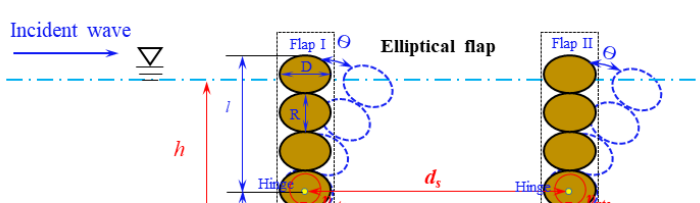
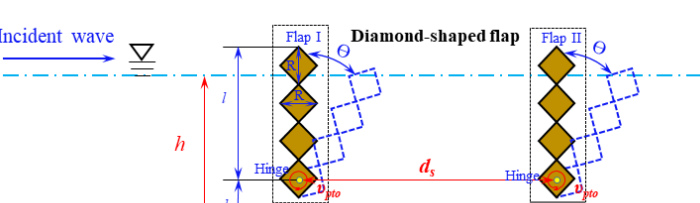
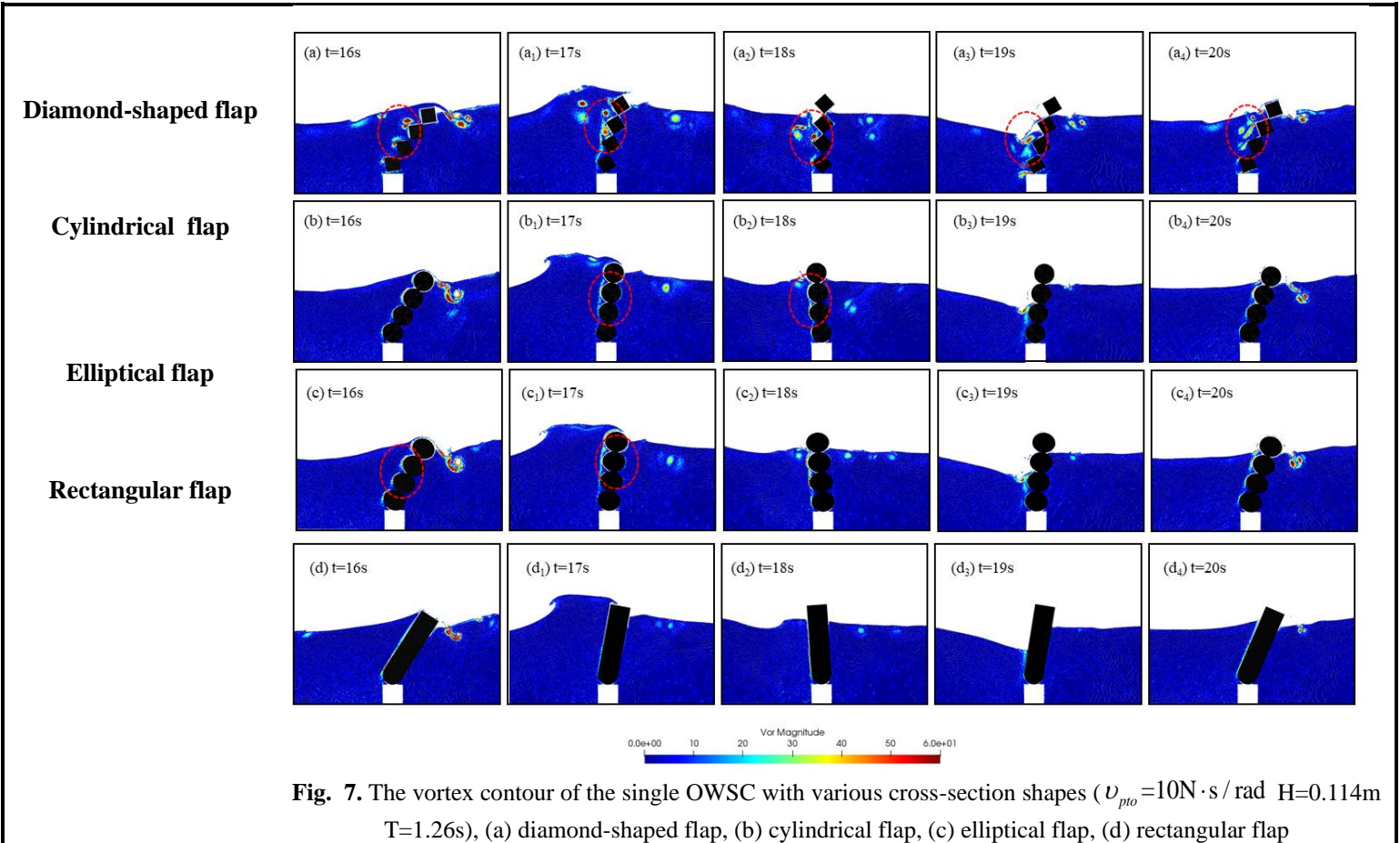
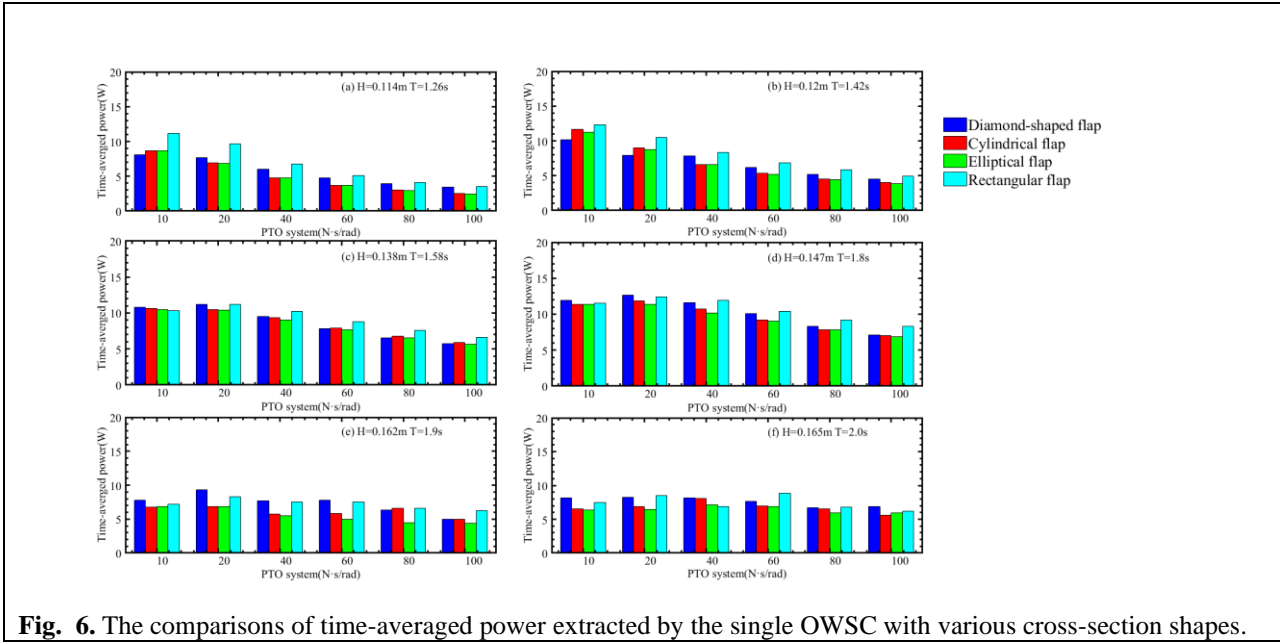
Propotype	Diagrammatic sketch	Cross-section shape
 <p>Oyster1(Whittaker and Folley, 2012)</p>		
 <p>Oyster800(Schmitt et al., 2016a)</p>		
 <p>1:25scale box-shapedflap model(Wei et al., 2015)</p>		
 <p>WAVEROLLER (Kasanen,2015. https://awenergy.com/waveroller/)</p>		

Table 3 Designed parameters for oscillating wave surge converter

Parameters	Values	Units	Cross-section shapes
Water depth (h)	0.358,0.448,0.538	m	 <p>Rotational inertia = $0.0456\text{kg}\cdot\text{m}^2$ (about the center in pitch) Rotational inertia = $0.1276\text{kg}\cdot\text{m}^2$ (about the hinge in pitch)</p>
Thickness (R)	0.0875	m	
Hinge height from the seabed (l_b)	0.135	m	
Distance between the hinge and the top (l)	0.31	m	
Linear PTO system (U_{pto})	10,20,40,60,80,100	$\text{N}\cdot\text{s}\cdot\text{rad}^{-1}$	 <p>Rotational inertia = $0.0385\text{kg}\cdot\text{m}^2$ (about the center in pitch) Rotational inertia = $0.1019\text{kg}\cdot\text{m}^2$ (about the hinge in pitch)</p>
Distance between the dual OWSCs (d_s)	$0.68\lambda, 1.0\lambda, 1.35\lambda$	m	
Rotation angle	θ	rad	
Long axis of the ellipse (D)	0.1	m	
			 <p>Rotational inertia = $0.0424\text{kg}\cdot\text{m}^2$ (about the center in pitch) Rotational inertia = $0.1114\text{kg}\cdot\text{m}^2$ (about the hinge in pitch)</p>
			 <p>Rotational inertia = $0.0236\text{kg}\cdot\text{m}^2$ (about the center in pitch) Rotational inertia = $0.0638\text{kg}\cdot\text{m}^2$ (about the hinge in pitch)</p>

4.1 The single OWSC with various cross-section shapes

In this section, the wave energy capture capability of the single OWSC is examined first. Fig. 6 demonstrates the time-averaged power captured by the 4 different devices. As indicated, the wave energy captured by the rectangular flap OWSCs outperformed the other cross-section shapes in most cases. Each sub-figure denotes a different wave condition, sub-figures in each row stand for the same water depth. For detailed water depth, refer to Table 1. Within each wave condition, different PTO damping levels from 10 to $100\text{ N}\cdot\text{s}/\text{rad}$ were examined.



Despite less vortex, the rectangular flap captured less power at some wave

periods than the other three flaps, see Fig. 7 for vortex contour. It may be because of the slight rotational inertia difference between the different flaps, although the materials remain the same in this research work. Just as shown in Table 1, it can be seen clearly that the rotation inertia about the hinge in pitch for the diamond-shaped flap is smaller than in other models. Apparently, in some instances, the flap rotation amplitude of the diamond-shaped flap is bigger than that of the cylindrical flap or elliptical flap, which can be attributed that the state of flap rotation is more easily to be changed than others under the inertia effect. In other words, when the same wave load exerting on the diamond-shaped flap, such a configuration can be turned at a larger angle than others.

Similarly, Fig. 6 also revealed that the immersed depth of the OWSCs structure greatly affected the wave energy capture performance of OWSCs. It is not hard to see that the wave energy capture ability of OWSCs is not improved with the increase of depth, although the incident wave energy is enhanced. Fig. 7 explains the reason for this phenomenon regarding the vortex field around the submerged part of the OWSCs with rectangular flap. It can be seen that more and more vortex structure attaches themselves to the top half of the flap with the increase of the water depth and incident wave energy. It should be noted that the turbulent motion plays a significant role in dissipating the wave energy into internal fluid energy. In that instance, according to energy conservation law, when the proportion of dissipated wave energy increases, the flap motion will certainly be affected, and its rotation amplitude will decrease.

In general, compared with other shapes, apart from simple manufacturing technology, convenient portability, and flexible use, the rectangular shape can be a good choice for the cross-section shape of a single OWSC due to its outer smoothed surface and better wave energy capture performance. In addition, the water depth plays a vital role in the wave energy capture capability of the single OWSC. The height of the OWSC is recommended to be higher than the water depth.

4.2 The dual OWSC with various cross-section shapes

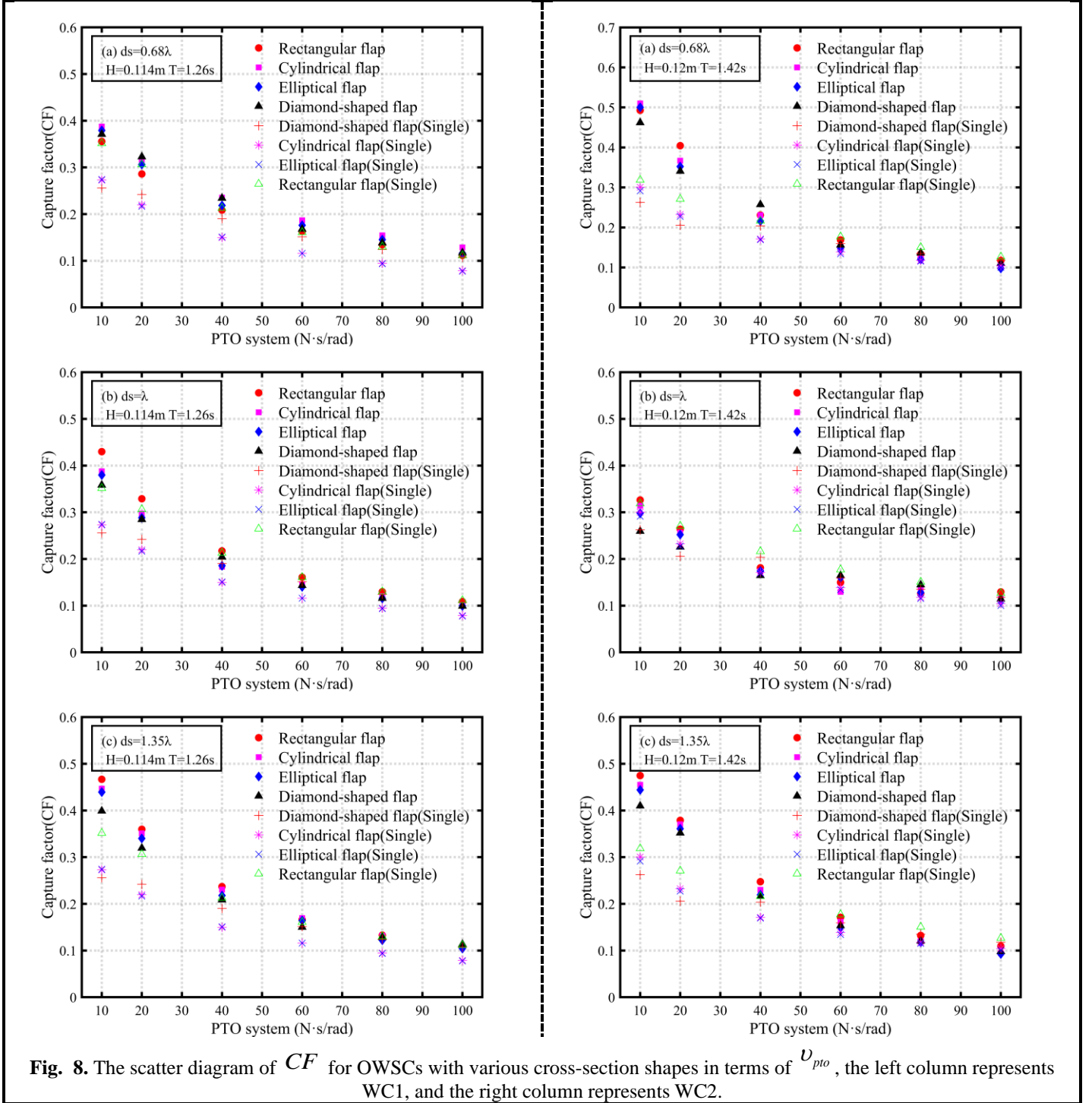
4.2.1 Case settings

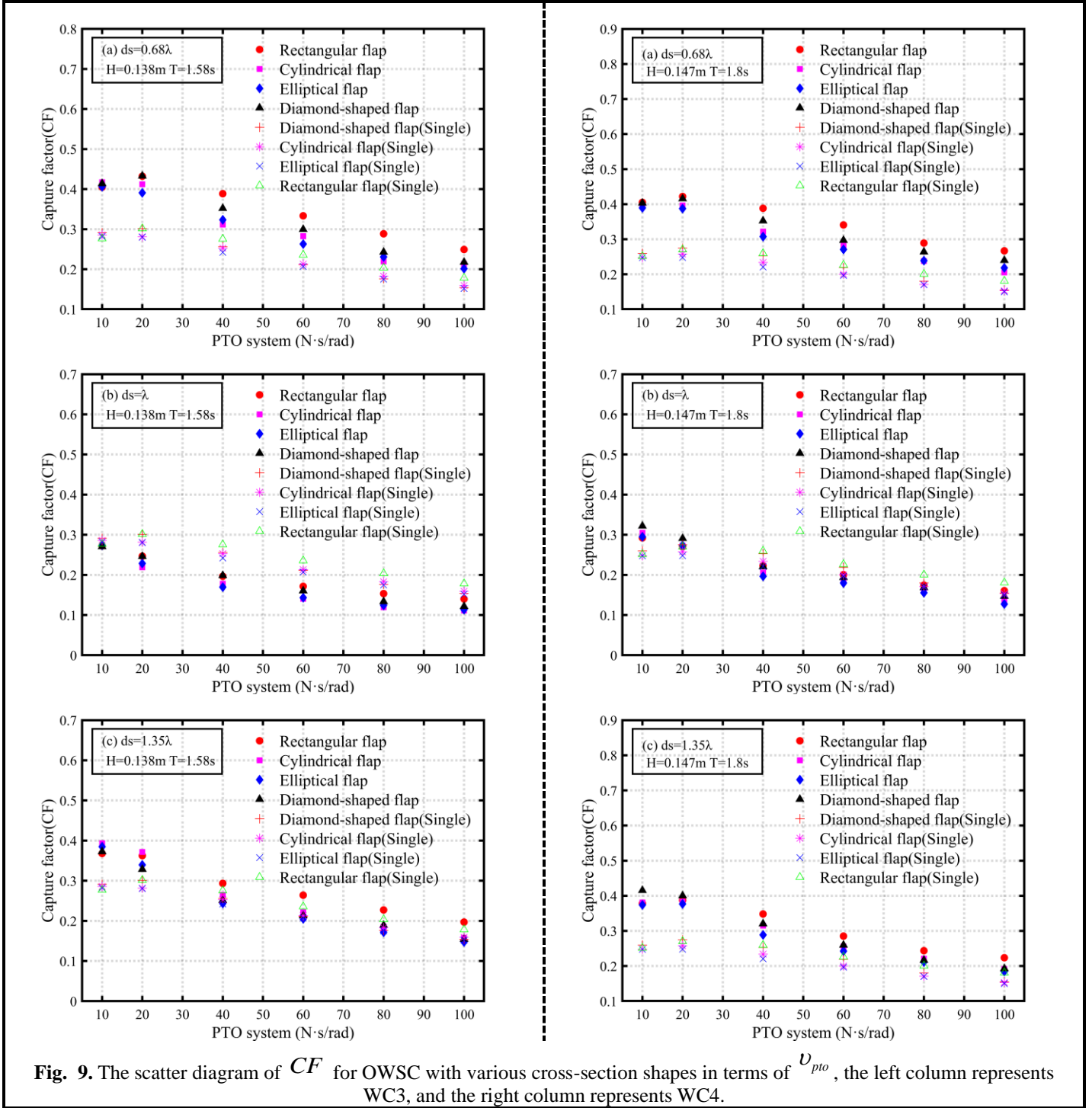
The wave capture performance of OWSC with various cross-section shapes was

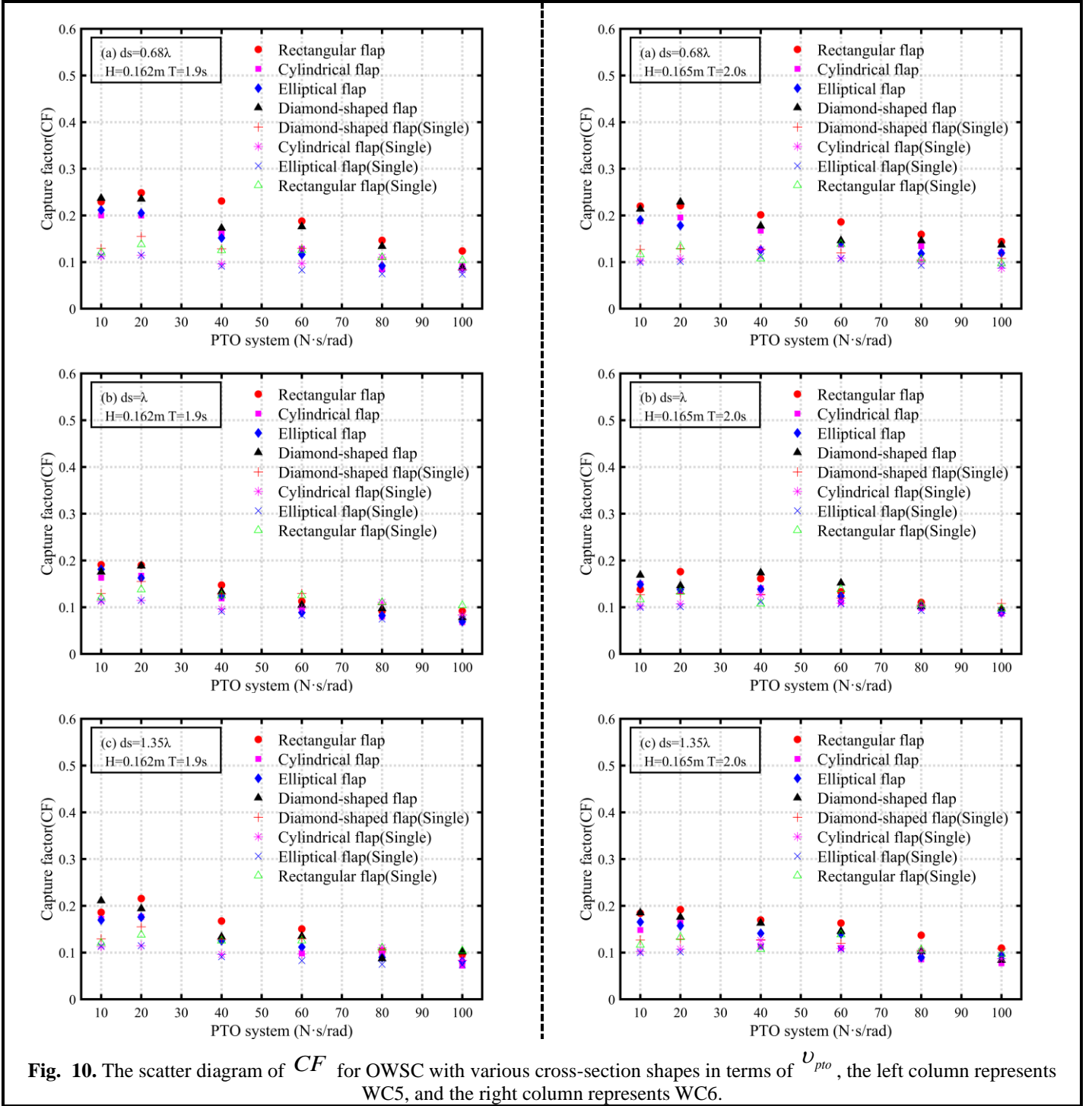
compared under different working conditions, including various water depths, different wave conditions, and different intervals. In this research work, a total of 576 cases were simulated, including 144 cases in a single OWSC numerical computation. Results are presented from Fig. 8. The scatter diagram of CF for OWSCs with various cross-section shapes in terms of U_{pto} , the left column represents WC1, and the right column represents WC2. to Fig. 13. The scatter diagram of P_e for each one of the OWSCs in the dual configuration with various cross-section shapes in terms of U_{pto} , the left column represents WC5, and the right column represents WC6..

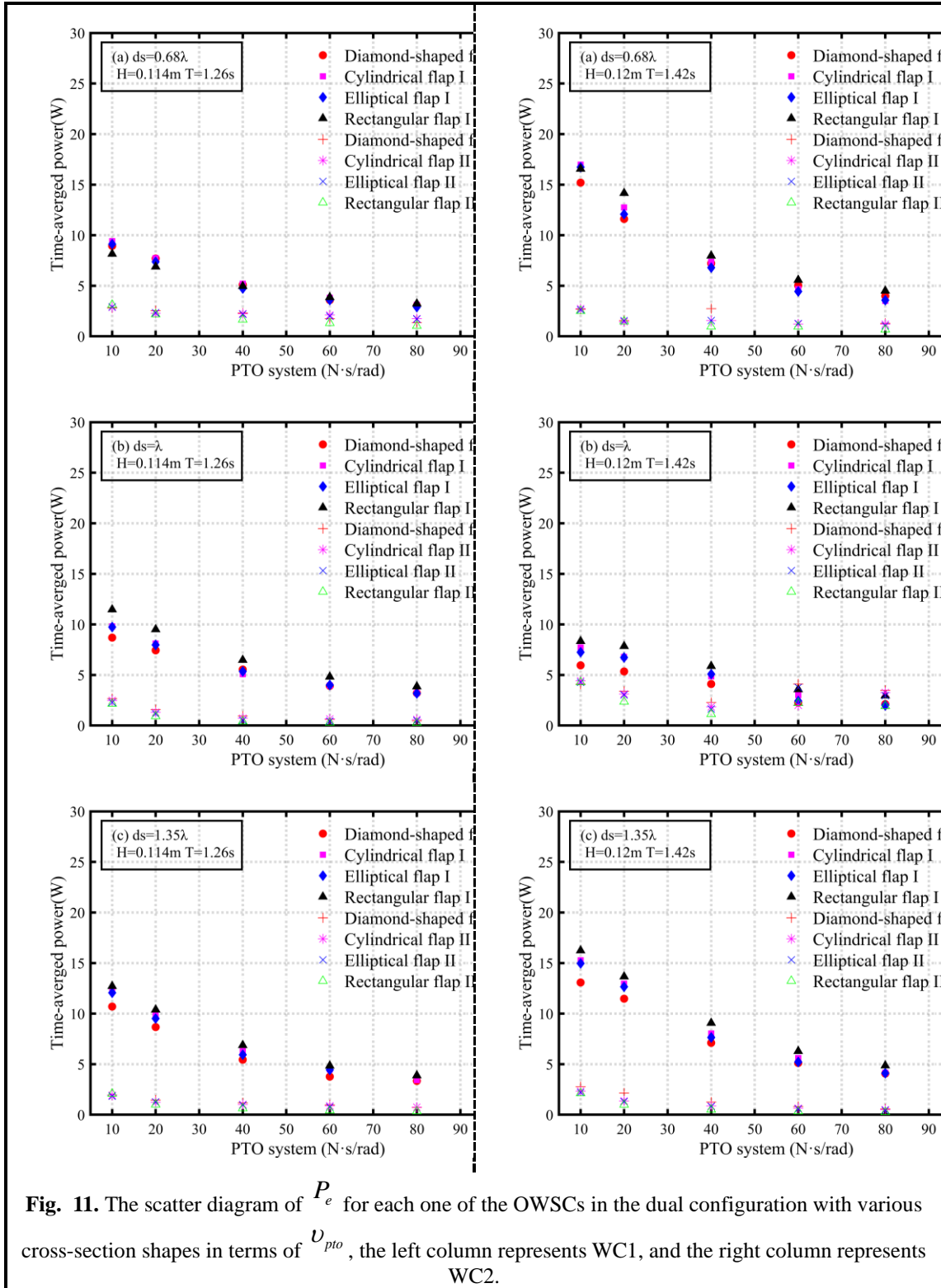
4.2.2 Numerical results and analysis

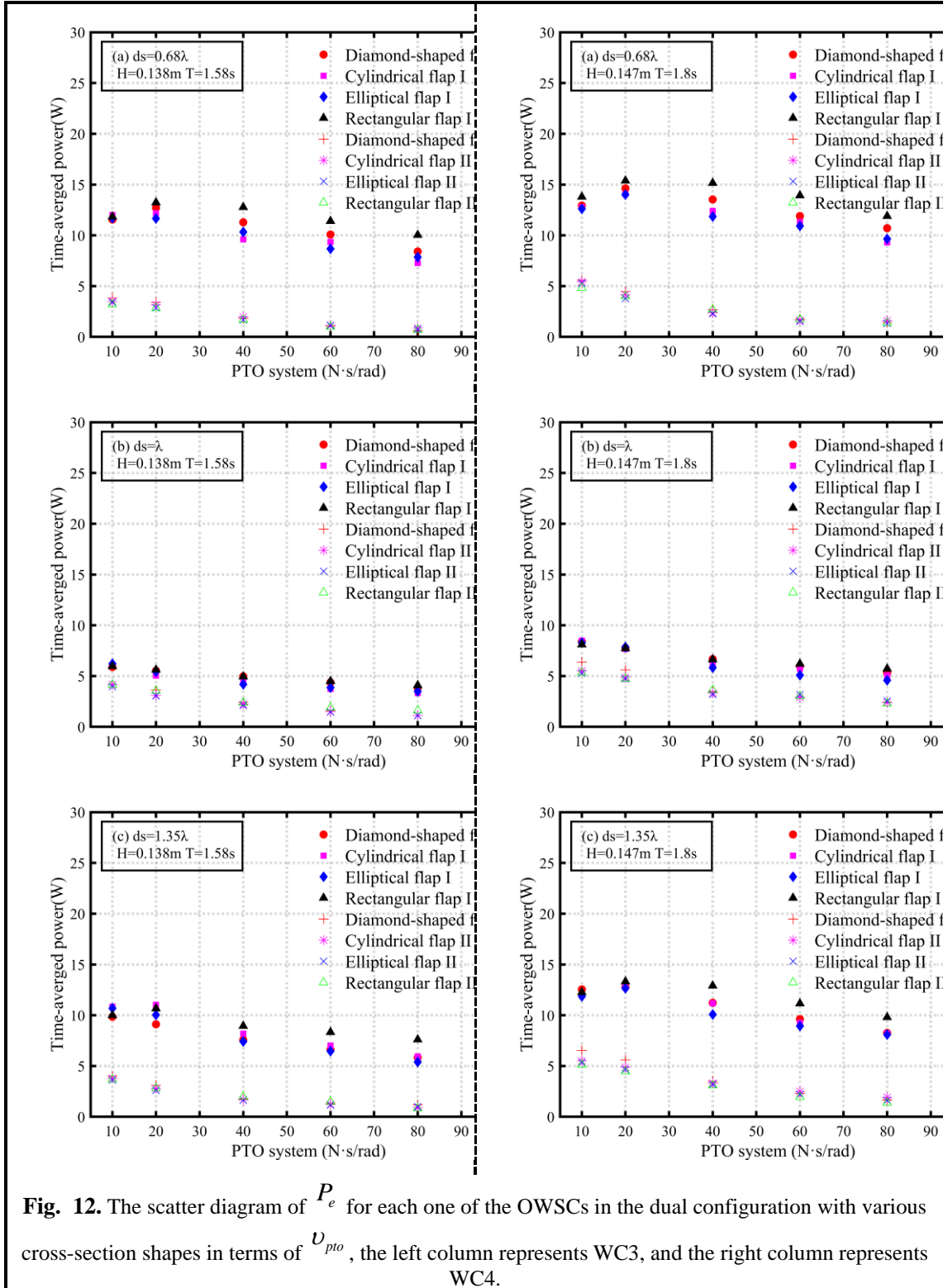
4.2.2.1 Numerical result











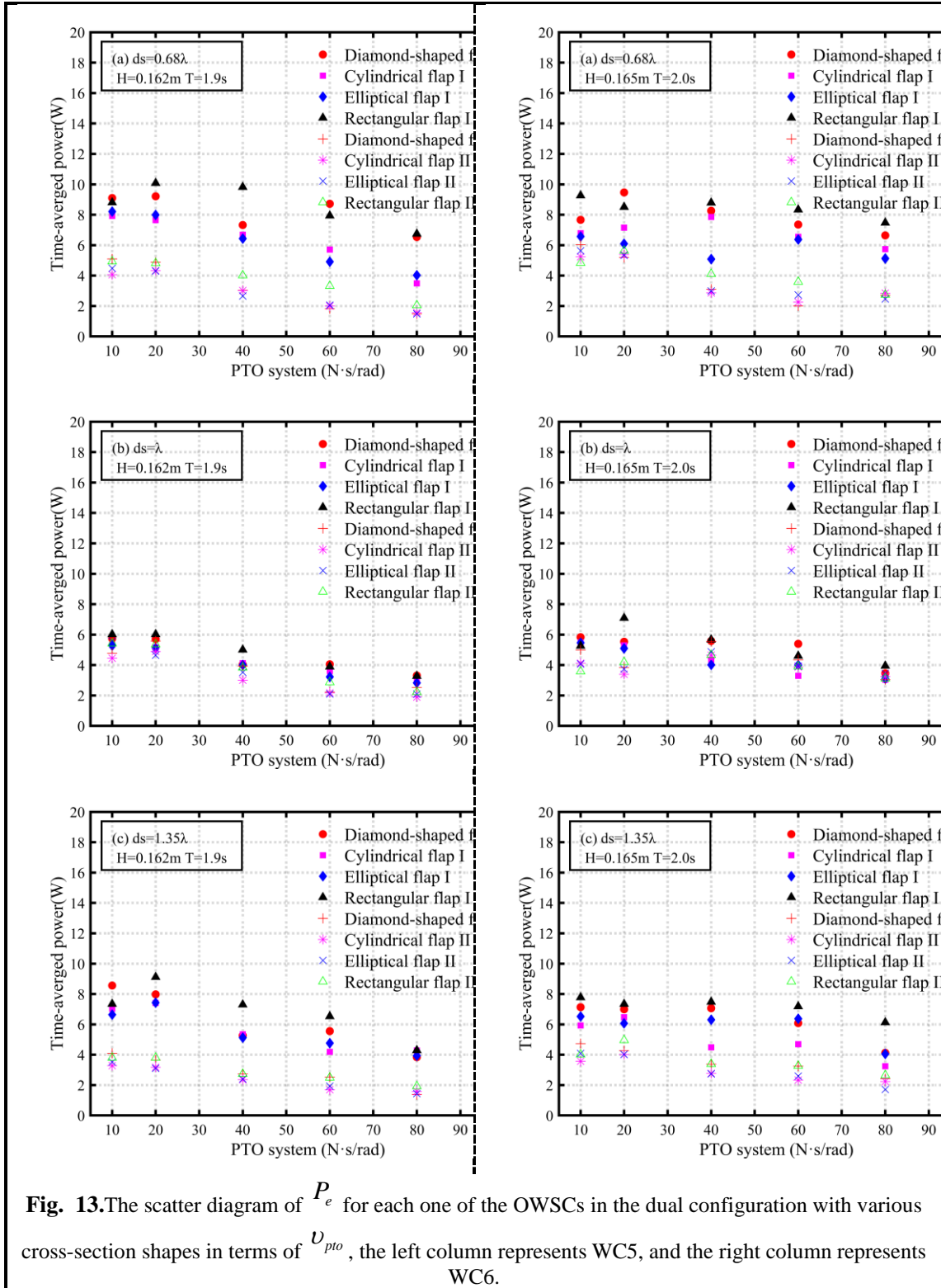


Fig. 8. The scatter diagram of CF for OWSCs with various cross-section shapes in terms of v_{pto} , the left column represents WC1, and the right column represents WC2.- Fig. 10. The

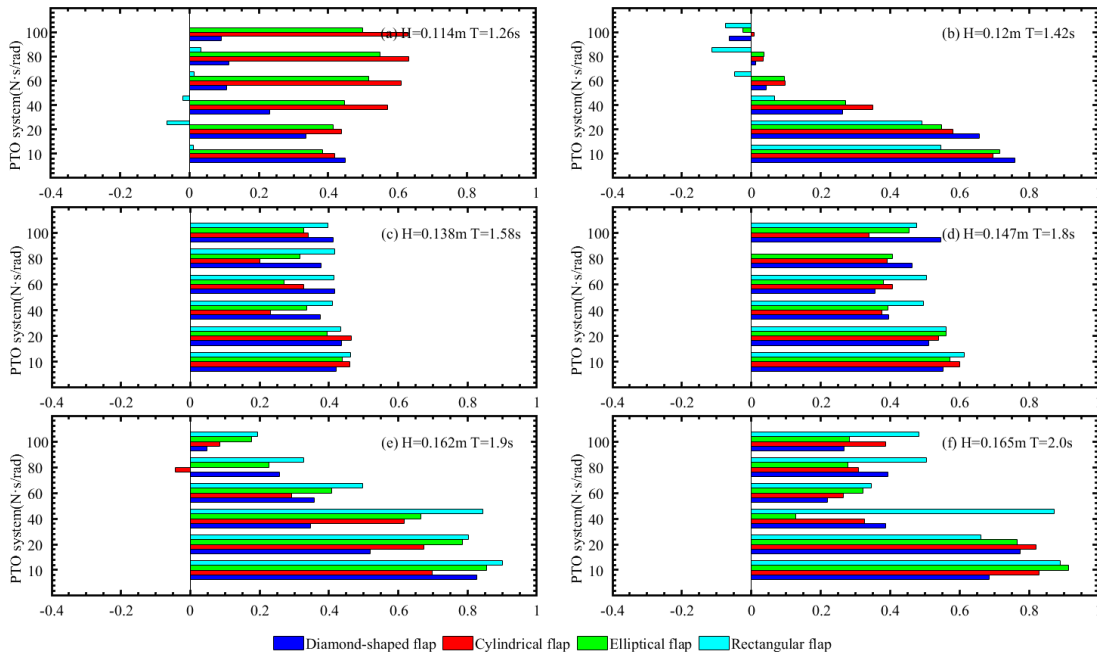
scatter diagram of CF for OWSC with various cross-section shapes in terms of U_{pto} , the left column represents WC5, and the right column represents WC6. shows the variation of CF for OWSCs with various cross-section shapes against different PTO damping U_{pto} . Each figure represents a combination of different wave conditions and dual OWSCs separations. In most cases, the capture factor of a dual OWSCs system is larger than that of a single OWSC. The existence of flap II can be helpful to the wave energy reuse at the lee side of flap I. When the wave reaches between flap I and flap II, the coupling interaction between the radiated wave from flap I and the second scattered wave can induce stronger wave resonance in this area. As suggested by the results, the interval between the two flaps makes an apparent effect on the wave energy extraction capability of dual OWSCs. Fig. 11- Fig. 13 presents the time averaged power generated by each one flap for the dual OWSCs. It can be seen clearly that in the case of dual OWSCs, flap I which is more close to wave maker is more efficient than flap II. Moreover, the difference in wave energy capture performance is not significant if the two flaps' distance is one wavelength.

The power extraction performance is enhanced when $d_s=0.68\lambda$ or $d_s=1.35\lambda$. while the enhancement is less pronounceable when the distance equals one wavelength. To be specific, according to Fig. 8- Fig. 10, when the gap between the two flaps is one wavelength, the total capture factor of dual OWSC is smaller than the other two intervals, especially for a low damping PTO. It should be also noted that if the two flaps' distance is one wavelength, the performance of dual OWSC is even worse than the single OWSC in some cases when the water depth is kept the same as the flap height. In addition, it can be observed that in most cases, the rectangular flap can perform better than other shapes, regardless of whether it is a dual OWSC or a single OWSC. Besides, water depth plays an important role. For the same cross-section shape, the capture factor CF shown in Fig. 8- Fig. 10 decreases with increasing depth, regardless of intervals between the two flaps. While for the same water depth, the wave energy extraction capability improved as incident wave energy increased. Likewise, according to the results shown in Fig. 10, the changes in the linear PTO

system have less effect on the capture factor CF when the water depth exceeds the flap height. While the capture factor CF depicted in Fig. 8 and Fig. 9 decreases with an increasing linear PTO system, which follows the same trend described by Liu et al.(2020). Finally, it is important to point out that for a single OWSC, the capture factor CF is never more than 0.5, which is consistent with the theoretical solution (Henry et al., 2018). Moreover, when U_{pto} changes from 10 to 40, the trend CF shown in Fig. 10 increases at the beginning and then decreases for all the models, meaning there exists optimum damping of PTO under the circumstances.

4.2.2.2 Result analysis

i. The comparison and analysis of the wave energy capture factor for single OWSC and dual OWSC



$$\left(P_{e(dual\ OWSCs)} - P_{e(single\ OWSC)} \right) / P_{e(single\ OWSC)} \%$$

Fig. 14. Contribution to the time-averaged power extracted from dual OWSCs with various cross-section shapes ($d_s=0.68\lambda$). The x -axes here represent the ratio of time averaged power increase. The positive value means the positive contribution while the negative values mean the negative contribution.

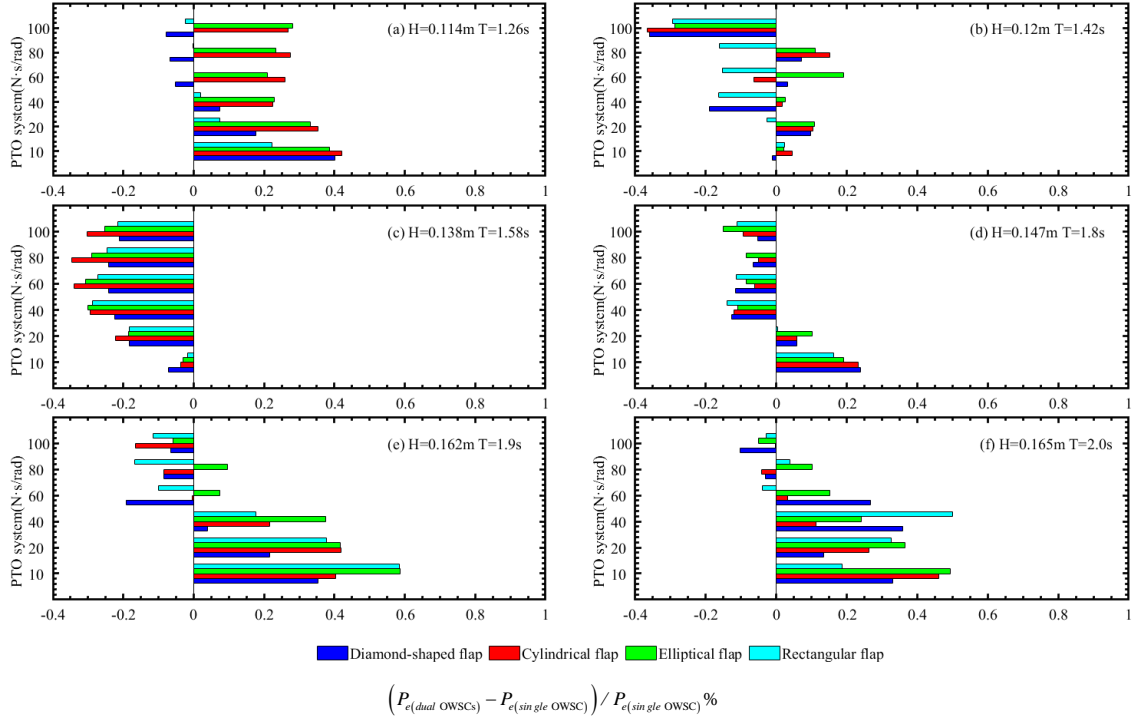


Fig. 15. Contribution to the time-averaged power extracted from dual OWSCs with various cross-section shapes ($d_s = \lambda$). The x -axes here represent the ratio of time averaged power increase. The positive value means the positive contribution while the negative value means the negative contribution.

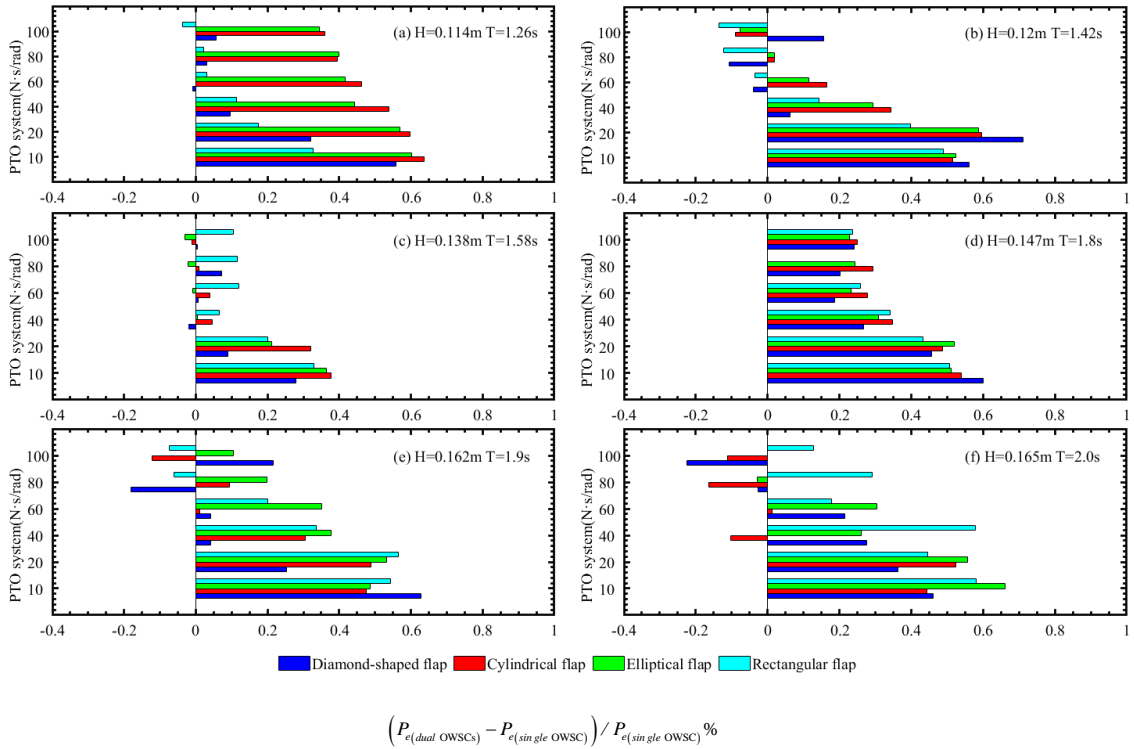
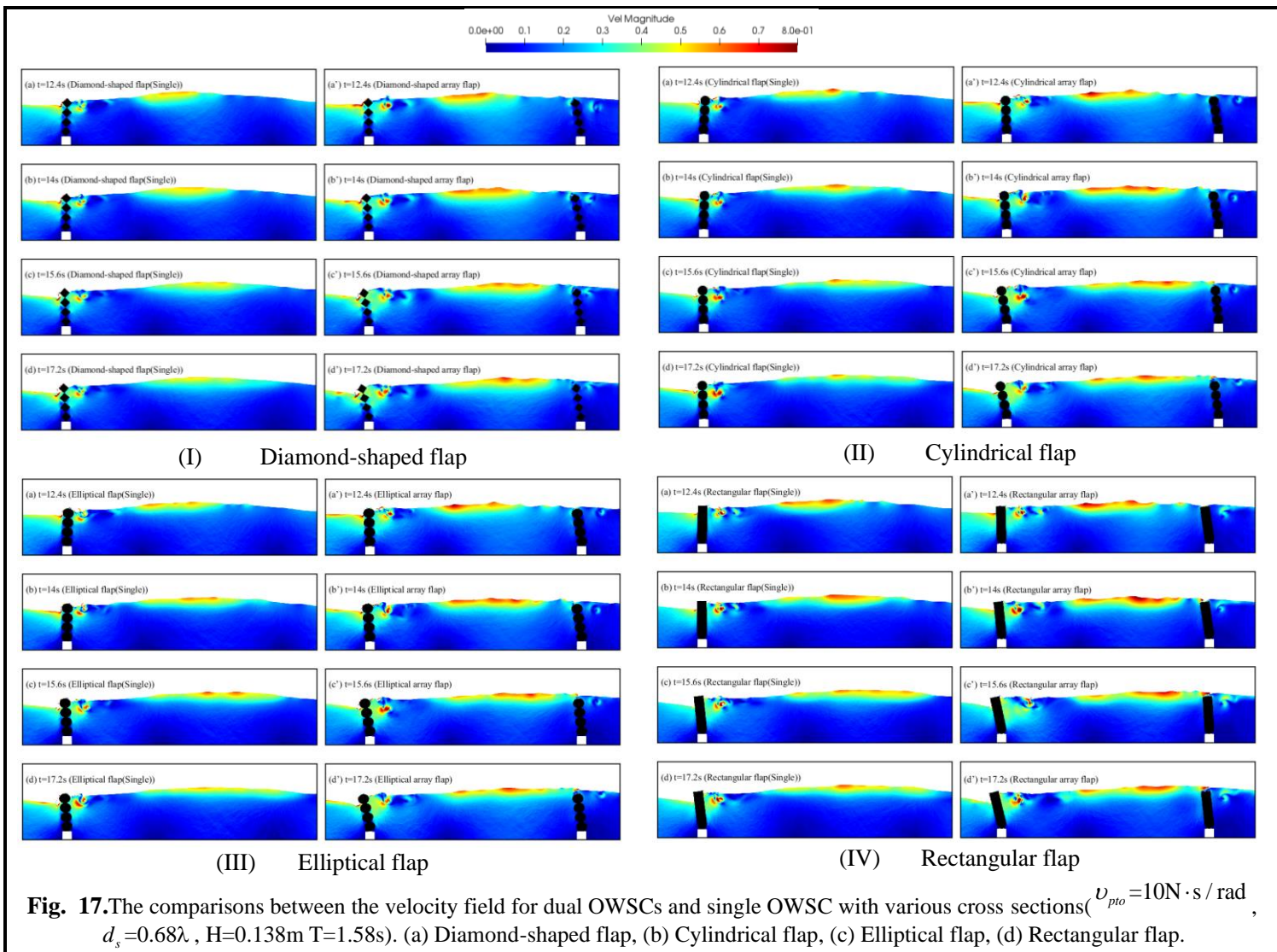


Fig. 16. Contribution to the time-averaged power extracted from dual OWSCs with various cross-section shapes ($d_s = 1.35\lambda$). The x -axes here represent the ratio of time averaged power increase. The positive value means the positive contribution while the negative value means the negative contribution.

As shown in Fig. 14-Fig. 16, in most cases, dual OWSCs positively contribute

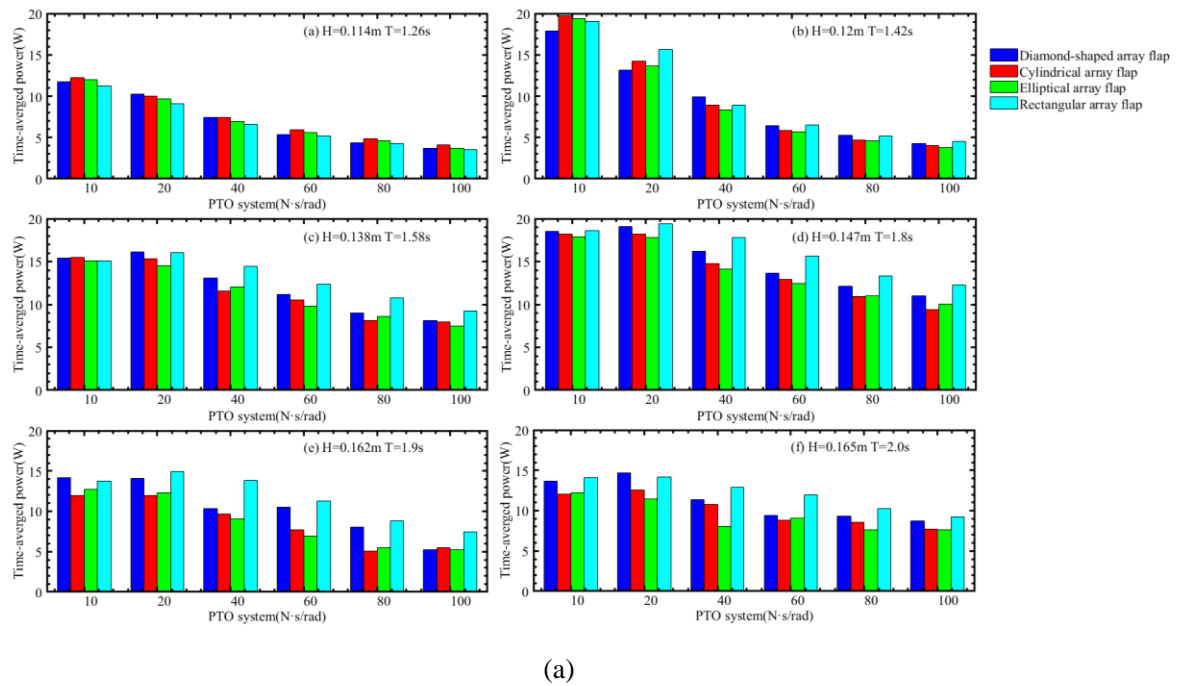
to improving the overall wave energy extraction. When the distance between the two flaps is one wavelength, the existence of two flaps gives less contribution to wave energy absorption, sometimes even negative. Take WC3 for example, the velocity field around the flap of dual OWSCs is shown in Fig. 17. For comparison, the velocity field of the corresponding single OWSC is also presented. Obviously, the presence of flap II can change the flow field between the two flaps, which can be exhibited qualitatively by the irregular fluid free-surface shape and complex velocity distribution of the flow. Just as depicted in Fig. 17, the radiated waves from flap I and the second-reflected wave interact between flap I and flap II. The strongly nonlinear interaction is evident by the visible double or more crests on the free surface between



the two flaps.

Overall, it can be concluded that dual OWSCs can perform better than a single OWSC in terms of power extraction, except when the interval between flap I and flap II is one wavelength. In addition, it can be concluded that the contribution to wave energy extraction is limited with the current array arrangement. The power captured by the current dual OWSCs is less than two individual single OWSCs would have captured.

ii. Various cross-section shapes effect



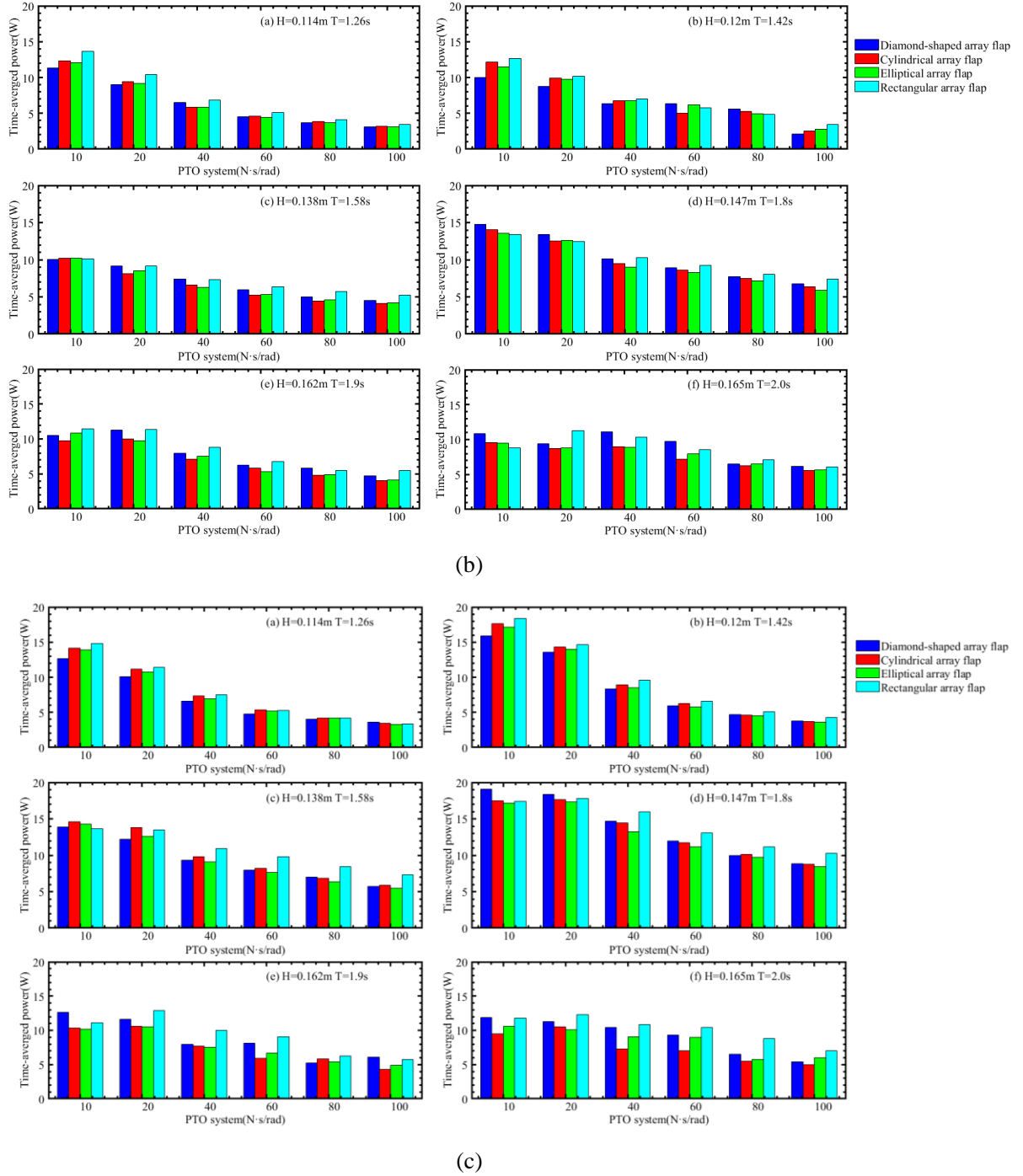


Fig. 18. The comparisons of time-averaged power extracted by the dual OWSC with various cross-section shapes, (a) $d_s=0.68\lambda$; (b) $d_s=\lambda$;(c) $d_s=1.35\lambda$

Fig. 18 presents the time-averaged power extracted by dual OWSCs with various cross-section shapes. Like the single OWSC device, the rectangular flap shows the best performance with good wave energy capture capability. The rectangular flap experienced the least vortex, similar to the single-unit device. The energetic vortices can bring remarkably negative effects on the moving performances of the flap structure. As the single flap shows, compared with other models, the

rectangular flap can effectively prevent a certain amount of fluid kinetic energy from transforming fluid into internal energy and extract more energy to intensify flap motion. Moreover, the rectangular flap has many other advantages, such as simple manufacture, better stability, good maintainability, and convenient deployment. In general, the rectangular flap can be a good choice for flap cross-section shapes.

iii. Flap interval effect analysis

As mentioned in Section 4.2.2.1, the intervals between the two flaps have a great effect on the wave energy extraction for the dual OWSCs. Take WC4 for example, Fig. 19 gives the time series of flap rotation for the two OWSCs, including the two rectangular flaps of dual OWSCs and the single rectangular flap OWSC. It can be found in Fig. 19 that a phase shift occurred between the flap I rotation and the flap II rotation for a dual OWSC when the two flaps interval equals one incident wavelength, which may be a contributory cause of wave energy extraction performance degradation problem. It is known to all that the flap motion phase differences can disturb wave propagation and force the wave to superpose onto each other. In this situation, flap II seems to work as a flap-type wavemaker. The generated waves (reflect and radiate waves) from flap II enlarged flap I's response. On the other hand, when flap II and flap I are moving in the same phase, flap I behaves more like a wave absorber. Fig. 20 compares the time history of flap rotation for all OWSCs.

Just as shown in Fig. 20, there is almost no visible motion phase difference between these OWSCs, whose cross-section areas are modelled by the same shapes. That is why if the two flaps' distance is one wavelength, the performance of dual OWSC is even worse than that of the two other intervals under the same wave condition, no matter which cross-section shapes are.

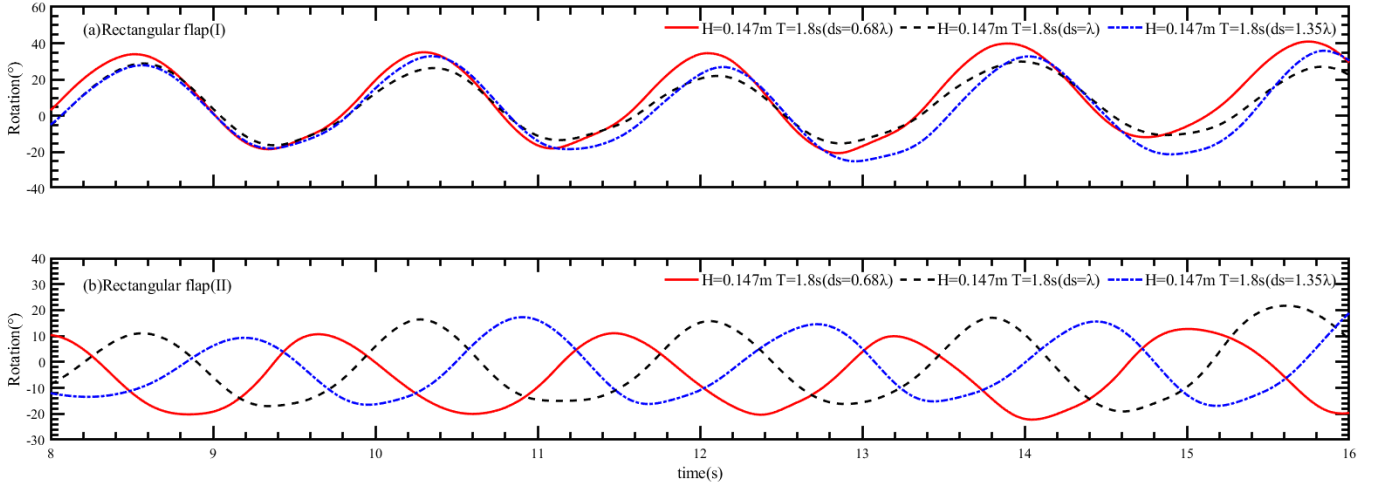


Fig. 19. The comparisons between the time of series of flap rotation for dual OWSCs with rectangular flap ($\nu_{pto}=10N \cdot s / rad$ $H=0.147m$ $T=1.8s$). (a) Flap I, (b) Flap II.

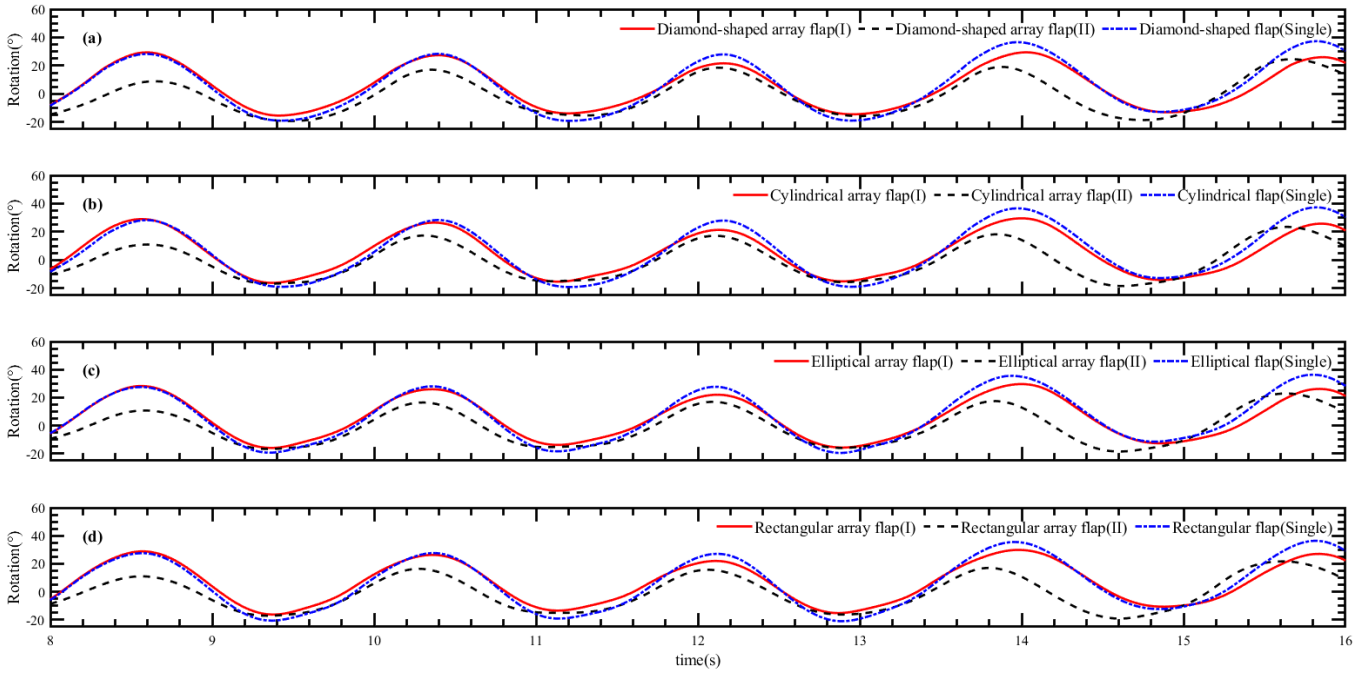


Fig. 20. The comparisons between the time of series of flap rotation for dual OWSCs and single OWSC with various cross-section shapes ($\nu_{pto}=10N \cdot s / rad$ $d_s=\lambda$ $H=0.147m$ $T=1.8s$). (a) Diamond-shaped flap, (b) Cylindrical flap, (c) Elliptical flap, (d) Rectangular flap.

iv. Water depth effect analysis

In this research work, another interesting note is that the wave absorption efficiency of the flap structure has no obvious improvement with the increase of incident wave energy. Due to the viscous effect, the entire OWSC system shows a lower efficiency of energy extraction despite larger wave amplitudes. On the contrary, the energy-capturing performance decreases with increasing water depth despite the increment in the incident wave energy. In the shallow water wave motion, the

amplitude of the horizontal velocity component of the fluid particle is constant along the water depth direction, and the amplitude of the vertical velocity component decreases linearly along the water depth direction. While in deep-water waves, the amplitude of the horizontal and vertical velocity components of water particles are roughly equal. Their magnitude decreases exponentially with the increase of water depth. In this research work, when the wave leans towards shallow water waves as water depth decreases, the flap undergoes more surge force from the wave, which can improve the wave energy extraction capability of OWSCs. Due to the significant decaying rate of fluid velocity along the water depth direction in the deep wave, only the upper end of the flap surface can effectively absorb the surge force. In that case, the wave-absorbing efficiency of the entire system is limited. Fig. 21 presents the time series of flap rotation for OWSC with rectangular flap, including flap I at the wave ward side, flap II at the lee side, and the single OWSC. To describe the reasons for these differences more intuitively, the comparisons of the velocity field and vortex field of dual OWSCs with rectangular flaps are shown in Fig. 22 and Fig. 23, respectively. It can be seen from Fig. 21 that the flap rotation amplitude increased by a limited amount despite the considerable increase in the incident wave energy.

The related causes can be perceived in Fig. 22. It is not hard to see that the frequent collisions of the fluid particles occur more often in front of the flap I and the velocity field of dual OWSC is smoother under the action of WC1, which is also proved by the vortex field correspondingly. However, when the submerged depth of the flap is not shallower than the water depth, more and more vortex structure occurs around the upper of the flap, and the two-dimensional flow field is turned out to be more complex, which has a large influence on energy extraction characteristic and rotation stabilisation of flap. It can be seen from Fig. 23 that more and more superposition of fluctuations with different scales occurs around the upper of the flap. The deeper the water, the more obvious is the superposition effect. Overall, as the fluid particles tend to move randomly, more and more wave energy is dissipated into fluid internal energy. In these circumstances, the disorder particle motions lead to much energy loss in wave energy extracted by OWSCs, which will confine its

application in a limited water depth.

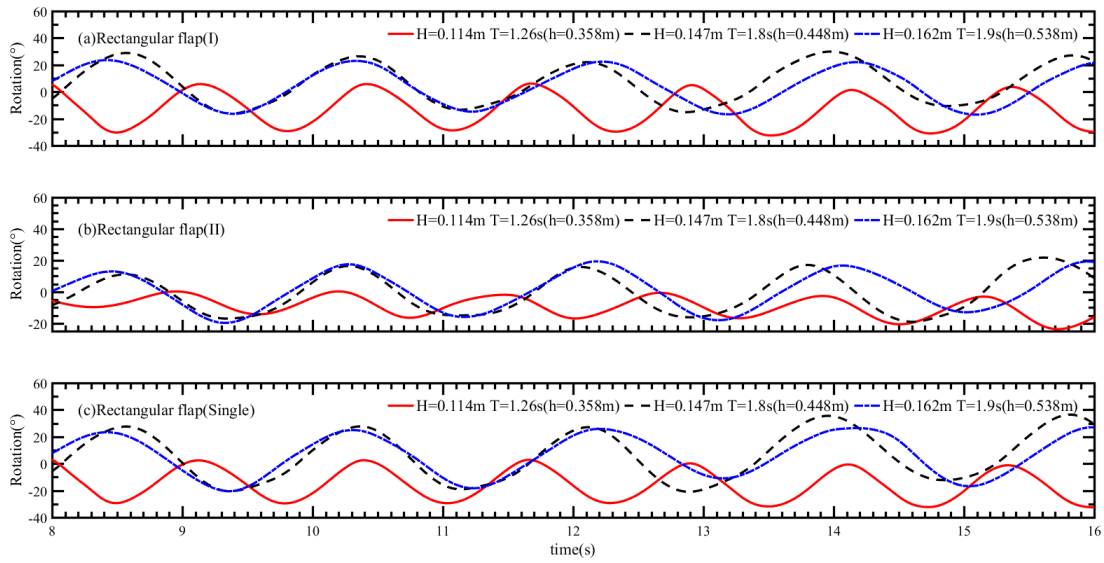
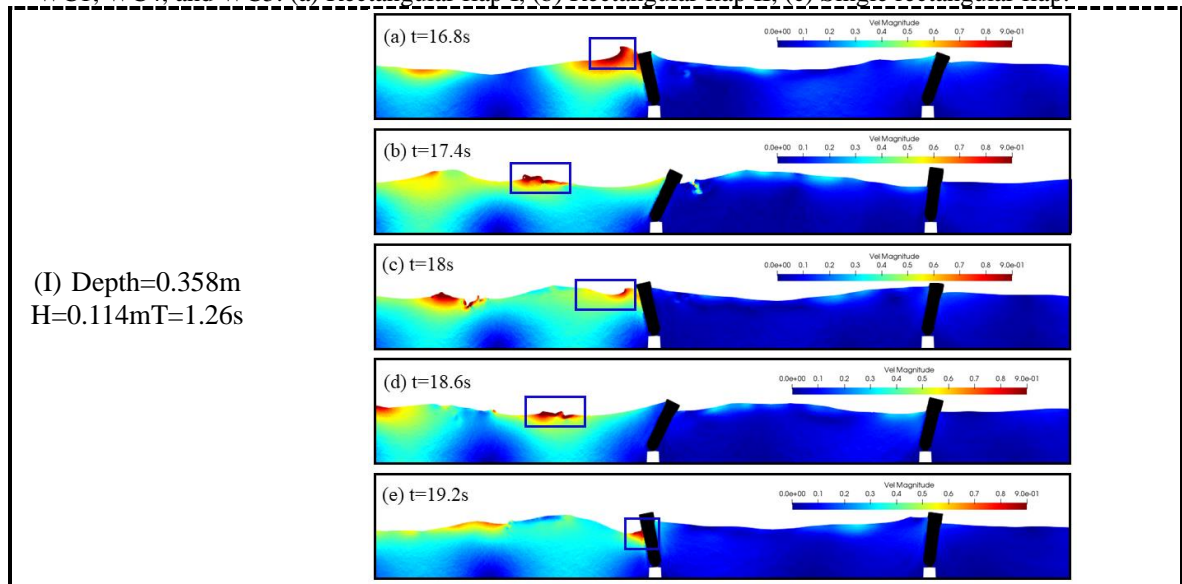


Fig. 21. The comparisons between the time of series of flap rotation for OWSC with rectangular flap ($v_{pto} = 10N \cdot s / rad$ $d_s = \lambda$) under WC1, WC4, and WC5. (a) Rectangular flap I, (b) Rectangular flap II, (c) Single rectangular flap.



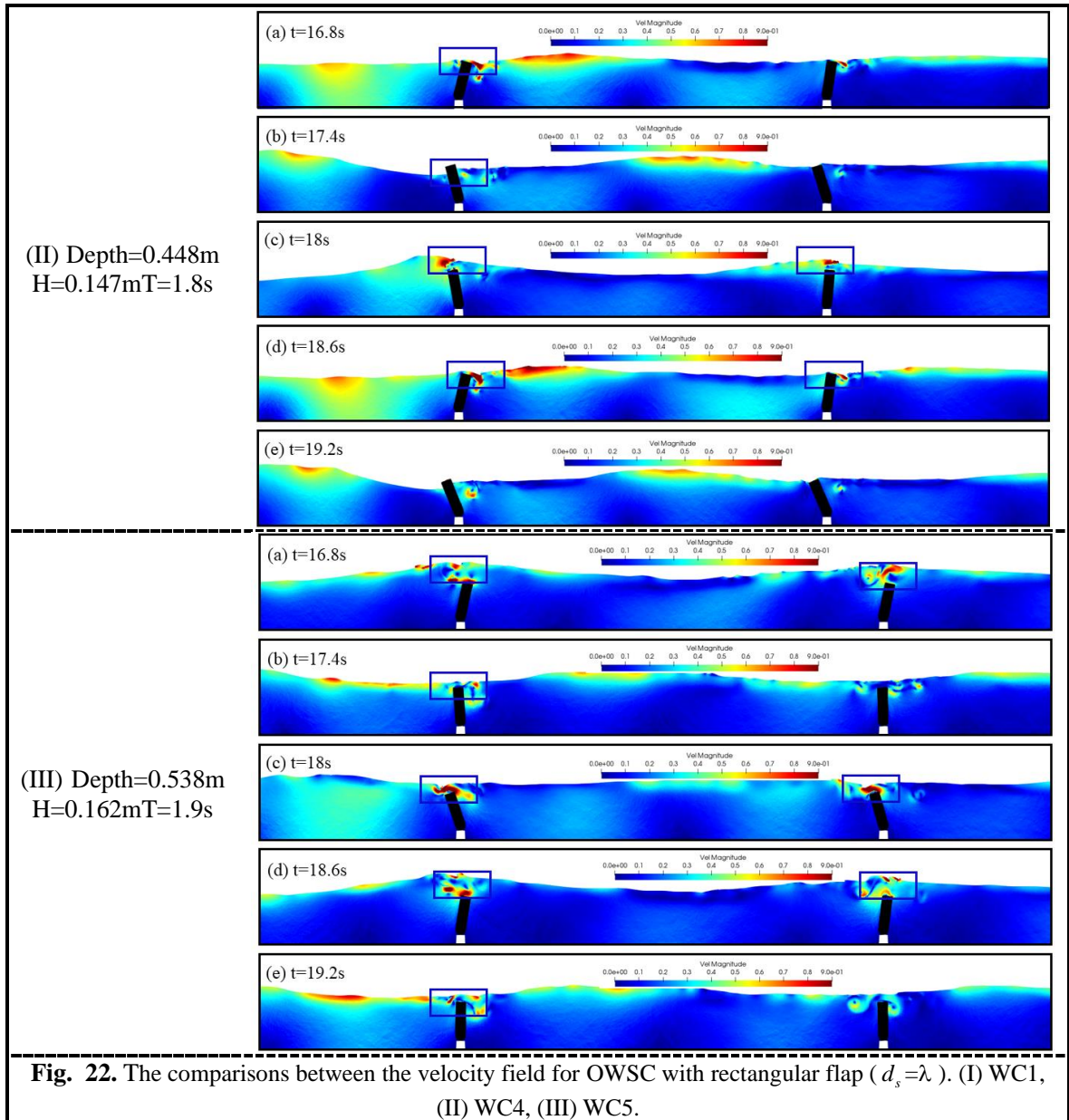
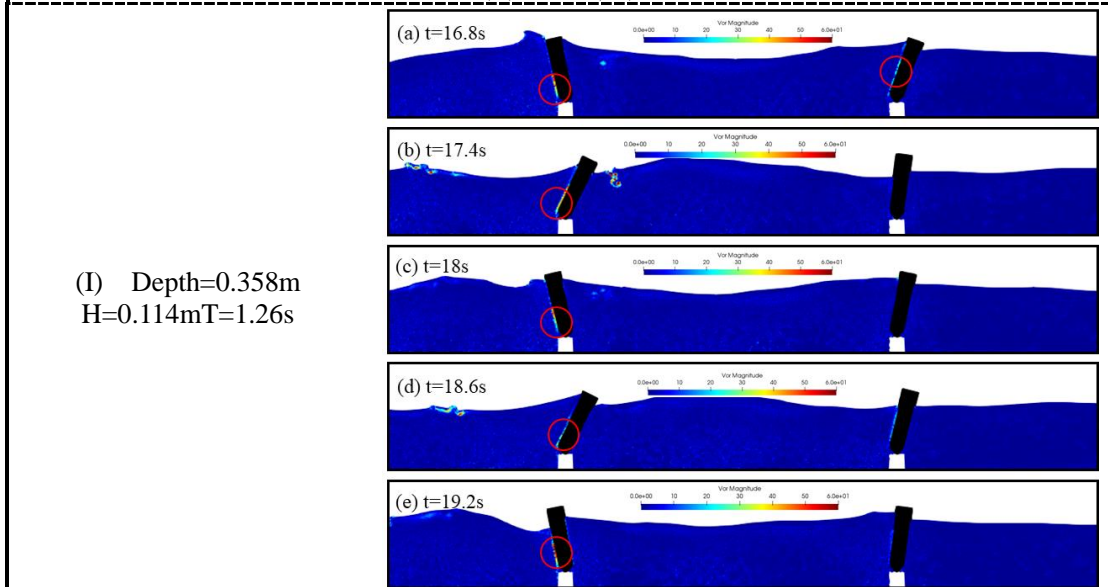


Fig. 22. The comparisons between the velocity field for OWSC with rectangular flap ($d_s = \lambda$). (I) WC1, (II) WC4, (III) WC5.





5. Conclusions

In this paper, a total of eight OWSC models with various cross-section shapes, including dual OWSCs and single OWSC were simulated using a coupled SPH model. At first, the coupling SPH model was verified by model experiments conducted by other scholars. Subsequently, the convergence analysis was organised to demonstrate the stability and accuracy of the coupling SPH model. After that, the related key parameters, such as the wave conditions, the distance between the two flaps, the working water depth, and the linear PTO damping, were also investigated to evaluate the differences in wave energy capture performances between the examined OWSC

models. The numerical results shown in this paper can provide a reference to parametric optimisation, for example, array configuration and cross-section shape design. Conclusions can be summarised as follows:

1. Compared to the other cross-section shapes, the rectangular flap has a better wave energy absorbing performance due to its smooth surface, which can reduce wave energy loss and enhance wave energy capture efficiency.
2. In most cases, the total mean wave power extracted by dual OWSCs is higher than that of a single OWSC. During this process, the interval between the two flaps plays a prominent role in wave absorption efficiency.
3. It should be noted that when the layout of the dual OWSCs is considered, the distance between the two flaps of a dual OWSCs should avoid being an integer number of wavelengths so that the two flaps will not operate in the same phase.
4. The total energy power extracted by OWSCs is greatly affected by the water depth for both the dual OWSCs and the single OWSC cases. For better absorption of incident wave energy, the flap height of OWSC should be greater than the water depth. In addition, if the water depth exceeds the flap height, there exists an optimum PTO damping that can capture the maximum amount of wave energy.

Compared to the single OWSC, the current arrangement of the two flaps for dual OWSCs shows significant improvements in the total wave energy extraction. However, the total power captured by the dual OWSCs is not higher than that would have been captured by two isolated single OWSCs, which makes the current OWSCs array configuration less favorable in terms of energy production. Nonetheless, the current configuration may still be economically viable if the spacing between the two flaps is short enough so that the cost of infrastructure, e.g., power transfer cable, can be significantly reduced. It is noticed that this research work is focused on two-dimensional cross-section numerical simulations for OWSCs. As a result, it is difficult to obtain the wave diffraction law and wave field evolution around the OWSCs. In addition, in a two-dimensional view, it is hard to figure out the variation of the wave field and wave energy extraction under the effect of staggered OWSCs. In future works, multi-GPU technology will be developed to accelerate the SPH code and

extend the computational domain size further, which can provide great assistance in simulating 3D OWSCs. After that, different configurations will be investigated in 3D simulation to explore some other configurations like staggered patterns.

Acknowledgment

This research work presented in this paper was supported by the Natural Science Foundation of China (Grant No. 51779111). The SPH code in this work was used based on the open-source code DualSPHysics (www.dual.sphysics.org) to which the authors are most grateful.

References

- Altomare C., Crespo A.J.C., Rogers B.D., Dominguez J.M, Gironella X., Gómez-Gesteira M., 2014. Numerical modelling of armour block sea breakwater with smoothed particle hydrodynamics. *Computers & Structures*. 130, 34-45.
- Altomare, C., Crespo, A.J.C., Domínguez, Jose M., Gomez-Gesteira, Moncho, Suzuki, T., Verwaest, T., 2015. Applicability of Smoothed Particle Hydrodynamics for estimation of sea wave impact on coastal structures. *Coast Eng.* 96,1–12.
- Altomare, C., Domínguez, J. M., Crespo, A. J. C., González-Cao, J., Suzuki, T., Gómez-Gesteira, M., & Troch, P., 2017. Long-crested wave generation and absorption for SPH-based DualSPHysics model. *Coastal Engineering*, 127, 37-54.
- Antuono, M., Colagrossi, A., Marrone, S., Lugni, C. 2011. Propagation of gravity waves through an SPH scheme with numerical diffusive terms. *Computer Physics Communications*, 182(4), 866-877.
- Antuono, M., Colagrossi, A., Marrone, S., Molteni, D. 2010. Free-surface flows solved by means of SPH schemes with numerical diffusive terms. *Computer Physics Communications*, 181, 532-549.
- Antuono, M., Colagrossi, A., Marrone, S. 2012. Numerical diffusive terms in weakly-compressible SPH schemes. *Computer Physics Communications*, 183, 2570-2580.
- Astariz, S., Iglesias, G., 2015. The economics of wave energy: A review. *Renew Sustain Energy Rev*, 45, 397–408.
- Babarit, A., 2015. A database of capture width ratio of wave energy converters. *Renewable Energy*, 80, 610-628.
- Becker, M., Teschner, M., 2007. Weakly compressible SPH for free surface flows. *Acm Siggraph/eurographics Symposium on Computer Animation*. DBLP.
- Batchelor, G.K., 1974. *Introduction to fluid dynamics*. Cambridge University Press. U.K.
- Brito, M., Canelas, R.B., García-Feal, O., Domínguez, J.M., Crespo, A.J.C., Ferreira, R.M.L., Neves, M.G., Teixeira, L., 2020. A numerical tool for modelling oscillating wave surge

- converter with nonlinear mechanical constraints. *Renew. Energy*. 146,2024–2043.
- Brito, M., Ferreira, Rui M. L., Teixeira, L., Neves, M., G., Canelas, R. B., 2020. Experimental investigation on the power capture of an oscillating wave surge converter in unidirectional waves. *Renewable Energy*, 151, 975-992.
- Canelas, R. B., Domínguez J. M., Crespo A.J.C., Gómez-Gesteira M., Ferreira R.M.L., 2015. A Smooth Particle Hydrodynamics discretisation for the modelling of free surface flows and rigid body dynamics. *International Journal for Numerical Methods in Fluids*, 78, 581-593.
- Canelas, R.B., Brito, M., Feal, O.G., Domínguez, J.M., Crespo, A.J.C.,2018. Extending DualSPHysics with a differential variational inequality: modeling fluid-mechanism interaction, *Appl. Ocean Res.* 76, 88-97.
- Caitlyn, E.C., Annalise, M., Bryony, D., P., 2019. An analytical cost model for co-located floating wind-wave energy arrays. *Renewable Energy*, 132, 885-897.
- Crespo, A.J.C., Gómez-Gesteira, M., Dalrymple, R.A., 2007. Boundary conditions generated by dynamic particles in SPH methods. *Computers, Materials & Continua*, 5, 173-184.
- Crespo, A.J.C., Domínguez, J.M., Rogers, B.D., Gómez-Gesteira, M., Longshaw, S., Canelas R.B., Vacondio, R., Barreiro, A., García-Feal, O., 2015. DualSPHysics: Open-source parallel CFD solver based on Smoothed Particle Hydrodynamics (SPH). *Computer Physics Communications*. 187,204-216.
- Crespo, A.J.C., Dominguez, J.M., Barreiro, A., Gómez-Gesteira, M. & Rogers, B.D., 2011. GPUs, a new tool of acceleration in CFD: Efficiency and reliability on Smoothed Particle Hydrodynamics methods. *PLoS ONE*, 6(6), e20685.
- Cheng, Y., Li, G., Ji, C.Y., Zhai, G.J., Oleg, G., 2018. Current effects on nonlinear wave slamming by an Oscillating Wave Surge Converter. *Engineering Analysis with Boundary Elements*, 96,150-168.
- Cheng, Y., Chen, X., Dai, S.S., Ji, C.Y., Cocard, M., 2021. Wave energy extraction for an array of dual-oscillating wave surge converters with different layouts. *Applied Energy*, 292,116899.
- Cui, J., Chen, X., Sun, P. N., 2021. Numerical investigation on the hydrodynamic performance of a new designed breakwater using smoothed particle hydrodynamic method. *Engineering Analysis with Boundary Elements*, 130, 379-403.
- Çelik, A., Altunkaynak, A. 2018. Experimental and analytical investigation on chamber water surface fluctuations and motion behaviours of water column type wave energy converter.

- Ocean Engineering, 150, 209-220.
- Domínguez, J.M., Crespo, A.J.C., Hall, M., Altomare, C., Wu, M., Stratigaki, V., Troch, P., Cappelletti, L., Gómez-Gesteira M., 2019. SPH simulation of floating structures with moorings. Coastal Engineering, 153, 103560.
- Greenwood, G., Christie, D., Venugopal, V., Morrison, J., 2016. Modelling performance of a small array of Wave Energy Converters: Comparison of Spectral and Boussinesq models. Energy, 113, 258-266.
- Gotoh, H., Khayyer, A., 2016. Current achievements and future perspectives for projection-based particle methods with applications in ocean engineering. Journal of Ocean Engineering and Marine Energy, 2(3), 251-278.
- Gómez-Gesteira, M., Rogers, B.D., Crespo, A.J.C., Dalrymple, R.A., Narayanaswamy, M., Domínguez, J.M., 2012. SPHysics – development of a free-surface fluid solver–Part1: Theory and formulations. Computers & Geosciences, 48, 289-299.
- Gunn, K., Stock-Williams, C., 2012. Quantifying the global wave power resource. Renew Energy, 44, 296-304.
- Gunawardane, S.D.G.S.P., Folley, M., Kankanamge, C.J., 2019. Analysis of the hydrodynamics of four different oscillating wave surge converter concepts, Renewable Energy, 130, 843-852.
- He, F., Zhang, H., Huang, C., & Liu, M., 2020. Numerical investigation of the solitary wave breaking over a slope by using the finite particle method. Coastal Engineering, 156, 103617.
- Henry, A., Rafiee, A., Schmitt, P., Dias, F., Whittaker, T., 2014a. The Characteristics of Wave Impacts on an Oscillating Wave Surge Converter. Journal of Ocean and Wind Energy, 1, 101-110.
- Henry, A., Kimmoun, O., Nicholson, J., Dupont, G., Wei, Y., Dias, F., 2014b. A two dimensional experimental investigation of slamming of an oscillating wave surge converter. In: Proceedings of the 24th International Offshore and Polar Engineering Conference, Busan, Korea, June. pp. 296–305.
- Henry, A., Folley, M., Whittaker, T., 2018. A conceptual model of the hydrodynamics of an oscillating wave surge converter. Renew. Energy 118, 963–972.
- Jiang, X., Day, S., Clelland, D., 2018. Hydrodynamic responses and power efficiency analyses of an oscillating wave surge converter under different simulated PTO strategies. Ocean

Engineering 170, 286-297.

Khayer, A., Shimizu, Y., Gotoh, H., Nagashima K., 2021. A coupled incompressible SPH-Hamiltonian SPH solver for hydroelastic FSI corresponding to composite structures. *Applied Mathematical Modelling*, 94, 242-271.

Kasanen, E. AW-Energy – Positive experiences of the Waveroller in Portugal and France. *WavEC Conference 2015, Lisbon*. <https://www.wavec.org/contents/files/04-aw-energy.pdf>.

Lind, S.J., Xu, R., Stansby, P.K., Rogers, B.D., 2012. Incompressible smoothed particle hydrodynamics for free-surface flows: A generalised diffusion-based algorithm for stability and validations for impulsive flows and propagating waves. *Journal of Computational Physics*, 231(4), 1499-1523.

Liu, Z.Q., Wang, Y.Z., Hua, X.G., 2021. Proposal of a novel analytical wake model and array optimisation of oscillating wave surge converter using differential evolution algorithm. *Ocean Engineering* 219, 108380.

Liu, Z.Q., Wang, Y.Z., Hua, X.G., 2020. Numerical studies and proposal of design equations on cylindrical oscillating wave surge converters under regular waves using SPH. *Energy Conversion and Management*, 203, 112242.

Marrone, S., Antuono, M., Colagrossi, A., Colicchio, C., Le, Touzé, D., Graziani, G., 2011. δ -SPH model for simulating violent impact flows. *Comput. Methods Appl. Mech. Engrg*, 200, 1526-1542..

Monaghan, J.J., 1989. On the problem of penetration in particle methods. *Journal of Computational Physics*, 82, 1–15.

Monaghan, J., 1992. Smoothed particle hydrodynamics. *Annu. Rev. Astron. Astrophys.*30 (1), 543–574.

Monaghan, J.J, Kos, A., 1999. Solitary waves on a Cretan beach. *Waterway Port. Coastal and Ocean Engineering*. 125, 145-154.

Mokos, A., Rogers, B.D., Stansby, P.K., 2016. A multiphase particle shifting algorithm for SPH simulations of violent hydrodynamics with a large number of particles. *Journal of Hydraulic Research*, 55:2, 143-462.

Madsen, O., 1971. On the generation of long waves. *Journal of Geophysical Research Atmospheres*, 76(36), 8672-8683.

Mazhar, H., Heyn, T., Negrut, D., Tasora, A., 2015. Using Nesterov's Method to Accelerate Multibody Dynamics with Friction and Contact. *ACM Trans. Graph.* 32,1-32,14.

Michele, S., Sammarco, P., d'Errico, M., Renzi, E., Abdolali, A., Bellotti, G., Dias, F. 2015. Flap

- gate farm: from Venice lagoon defense to resonating wave energy production. Part2: Synchronous response to incident waves in open sea. *Appl. Ocean Res.* 52, 43–61.
- Michele, S., Sammarco, P., d'Errico, M., 2016a. Theory of the synchronous motion of an array of floating flap gates oscillating wave surge converter. *Proc. R. Soc. Lond. Ser. A Math. Phys. Eng. Sci.* 472, 20160174.
- Michele, S., Sammarco, P., d'Errico, M., 2016b. The optimal design of a flap gate array in front of a straight vertical wall: Resonance of the natural modes and enhancement of the exciting torque. *Ocean Eng.* 118, 152–164.
- Michele, S., Renzi, E., Sammarco, P., 2018a. A second-order theory for wave energy converters with curved geometry. In: *Proc. 33rd Int. Workshop on Water Waves and Floating Bodies*, Guidel-Plages, France, 4-7 2017. pp. 137–140.
- Michele, S., Renzi, E. 2019. A second-order theory for an array of curved wave energy converters in open sea. *Journal of Fluids and Structures*, 88, 315-330.
- Michele, S., Sammarco, P., d'Errico, M., 2018b. Weakly nonlinear theory for oscillating wave surge converters in a channel. *J. Fluid Mech.* 834, 55–91.
- Michele, S., Renzi, E., Sammarco, P., 2019. Weakly nonlinear theory for a gate-type curved array in waves. *J. Fluid Mech.* 869, 238–263.
- Netbuoy, 2021, <https://www.netbuoy.co.uk/>, accessed on 20th Nov 2021.
- O'Brien, L., Christodoulides, P., Renzi, E., Stefanakis, T., Dias, F., 2015. Will oscillating wave surge converters survive tsunamis? *Theoretical and Applied Mechanics Letters*, 5,160-166.
- Project Chrono, 2018. <https://projectchrono.org/>. (Accessed 15 July 2020).
- Randles, P.W., Libersky, L.D., 1996. Smoothed particle hydrodynamics: some recent improvements and applications. *Comput. Methods Appl. Mech. Engng.* 139, 375–408.
- Renzi, E., Wei, Y., Dias, F., 2018. The pressure impulse of wave slamming on an oscillating wave energy converter. *Journal of Fluids and Structures*, 82, 258-271.
- Renzi, E., Abdolali, A., Bellotti, G., Dias, F., 2014. Wave-power absorption from a finite array of oscillating wave surge converters. *Renewable Energy*, 63, 55-68.
- Schmitt, P., Windt, C., Nicholson, J., Elsäßer, B., 2016a. Development and validation of a procedure for numerical vibration analysis of an oscillating wave surge converter. *European Journal of Mechanics B/Fluids*, 58,9-19.

- Schmitt, P., Asmuth, H., Elsäßer, B., 2016b. Optimising power take-off of an oscillating wave surge converter using high fidelity numerical simulations. *International Journal of Marine Energy*, 16,196-208.
- Sun, P.N., Colagrossi, A., Marrone, S., Antuono, M., Zhang, A.M., 2018. Multi-resolution Delta-plus-SPH with tensile instability control: towards high Reynolds number flows. *Comput. Phys. Comm.* 224, 63–80.
- Sun P.N., Le Touzé D., Zhang A.M., 2019. Study of a complex fluid-structure dam-breaking benchmark problem using a multiphase SPH method with APR. *Engineering Analysis with Boundary Elements*, 104, 240-258.
- Sun P.N., Le Touzé D., Oger G., Zhang A.M.,2021. An accurate FSI-SPH modeling of challenging fluid-structure interaction problems in two and three dimensions. *Ocean Engineering*, 221:108552.
- Simonetti, I., Cappiotti, L., Elsafti, H., Oumeraci, H., 2018. Evaluation of air compressibility effects on the performance of fixed OWC wave energy converters using CFD modelling. *Renewable Energy*, 119, 741-753.
- Tasora, A., Serban, R., Mazhar, H., Pazouki, A., Melanz, D., Fleischmann J.,Taylor M., Sugiyama H., Negrut D.,2016. Chrono: an open source multi-physics dynamics engine, in: *Lecture Notes in Computer Science*, Springer International Publishing, 19-49.
- Tay, Z. Y., Venugopal, V., 2017. Hydrodynamic interactions of oscillating wave surge converters in an array under random sea state. *Ocean Engineering* 145, 382-394.
- Wei, Y.J., Rafiee, A., Henry, A., Dias, F., 2015. Wave interaction with an oscillating wave surge converter, Part I: Viscous effects. *Ocean Engineering*, 104, 185-203.
- Wei, Y.J., Abadie, T., Henry, A., Dias, F., 2016. Wave interaction with an oscillating wave surge converter, Part II: Slamming. *Ocean Engineering*, 113, 319-334.
- Wang, L., Khayyer, A., Gotoh, H., Jiang, Q., Zhang, C., 2019. Enhancement of pressure calculation in projection-based particle methods by incorporation of background mesh scheme. *Applied Ocean Research*, 86, 320-339.
- Wang, R. Q., Ning, D.Z., Zhang, C.W., Zou, Q.P., Liu, Z. 2018. Nonlinear and viscous effects on the hydrodynamic performance of a fixed OWC wave energy converter. *Coastal Engineering*, 131, 42-50.
- Whittaker, T., Folley, M. 2012. Nearshore oscillating wave surge converters and the development of Oyster[J]. *Philosophical Transactions*, 370(1959):345.
- Ye T., Pan D., Huang C., Liu M., 2019. Smoothed particle hydrodynamics (SPH) for complex

fluid flows: Recent developments in methodology and applications. *Physics of Fluids* 31 (1), 011301.

- Zhang, C., Rezavand, M., Zhu, Y. J., Yu, Y. C., Wu, D., Zhang, W. B., Wang, J. H., Hu, X. Y., 2021. SPHinXsys: An open-source multi-physics and multi-resolution library based on smoothed particle hydrodynamics. *Computer Physics Communications*, 267, 108066.
- Zhang, D. H., Shi, Y. X., Huang, C., Si, Y. L., Huang, B., Li, W., 2018. SPH method with applications of oscillating wave surge converter. *Ocean Engineering* 152,273-285.